*Journal of Structural Dynamics*, 4, (pp. 74-103) 2026
Optimal damping compensation of a dynamic vibration absorber using an electromagnetic resistive shunt

Journal of Structural Dynamics

CC BY

# Optimal damping compensation of a dynamic vibration absorber using an electromagnetic resistive shunt

Guillaume Hay [*1], Christophe Giraud-Audine [†2], Hervé Mahé[3], and Olivier Thomas [‡1]

[1] *Arts et Metiers Institute of Technology, LISPEN, 8 Bd Louis XIV, 59000, Lille,France*
[2] *Arts et Metiers Institute of Technology, Univ. Lille, Centrale Lille, HEI, L2EP,8 Bd Louis XIV,59000, Lille, France*
[3] *Valeo Transmission, NeMo (New Mobility Center), 81 Ave Roger Dumoulin, 80009, Amiens,France*

## Abstract

This study focuses on the addition of an electromagnetic (EM) resistive shunt (R-shunt) to a standard mechanical Dynamic Vibration Absorber (DVA) to replace, compensate or tune its damping element. The R-shunt is placed between the mass of the DVA and the host structure. The inclusion of the R-shunt introduces an additional pole in the frequency response function of the host structure, resulting in three fixed points. Analysing these fixed points enables the optimisation of the absorber with the objective of minimising the $H_\infty$-norm of both displacement and acceleration of the structure. In both cases, a thorough optimisation of the obtained DVA+R-shunt absorber, in terms of mass ratio, electromagnetic coupling factor (EMCF) and electric resistance, is proposed. The response of this absorber is then compared to that of an optimised standard DVA, leading to equivalent performance when the parameters are correctly chosen. For optimal performance, the DVA must be detuned with respect to standard optimisation and the EMCF of the R-shunt must be adjusted to an optimal value, contrary to standard shunts where the performance often increase as a function of the EMCF. Finally, an experimental study validates the effectiveness of the proposed device.

**Keywords:** Dynamic vibration absorber; Electromagnetic shunt; Damping compensation

*Received on November 20, 2025, Accepted on September 24, 2026, Published on October 1, 2026*

## 1 Introduction

Mechanical structures often exhibit vibrations that can cause noise, fatigue or even failure. A classical passive solution is the Lanchester damper, which employs an inertia connected to the vibrating (primary) structure through a dashpot to dissipate its vibrations [1, 2, 3]. Better performance can be achieved with a Dynamic Vibration Absorber (DVA), also called a Tuned Mass Damper, that consists in connecting a mechanical resonator to the primary structure. It acts by both counteracting the oscillation of the primary structure and dissipating the energy thanks to its dashpot [4, 2]. The DVA basically adds a pole and a zero in the transfer function of the system, thus replacing the targeted resonance by an antiresonance at its natural frequency and two side resonances. In the case of a single frequency excitation, the antiresonance can be tuned to cancel the primary system's oscillations at this frequency, a property exploited in order tuned centrifugal absorbers for rotating machinery [5], or their electromagnetic equivalents [6, 7]. Those absorbers need to be as non-dissipative as possible for efficiency. On the contrary, for broadband excitation, the damping ratio of the DVA must be adjusted to mitigate the side resonances [8, 9]. In practice, damping in the DVA may be brought by several technologies. In civil engineering applications, DVAs are damped by oil dampers or viscoelastic materials [10]. In the case of tuned liquid absorbers, energy is dissipated while water passes through a calibrated orifice, in civil engineering or marine applications [10, 11]. Other architectures use dry friction dampers in

[*] guillaume.hay@ensam.eu
[†] christophe.giraud-audine@ensam.eu
[‡] olivier.thomas@ensam.eu

the form of a stranded cable, such as in Stockbridge dampers for electric transmission lines [12] or for Lanchester dampers [3]. Smaller size DVAs can also be considered [13, 14], especially for vibroacoustic applications [15]. In all those applications, the tuning of the DVA damping ratio may be challenging and mistuning has the potential to substantially diminish performance. In the case of dry friction element, their inherent nonlinear properties lead to amplitude dependent responses. The present paper proposes a solution to replace, compensate or tune the damping element of the DVA, by adding an electromagnetic resistive shunt between the DVA and the primary structure.

Electromagnetic shunts are part of the wider family of electromechanical shunts. The principle is to couple the vibrations of the primary structure to an electric circuit through an electromechanical transducer. The transducer converts mechanical energy into electrical energy, which can then be dissipated by a resistor. In this way, a simple resistive shunt acts as the electrical analogue of a mechanical damper. Pioneering work on electromechanical shunts has been carried out using piezoelectric transducers [16, 17]. In this instance, an inductor is connected to the terminals of the transducer, in addition to a resistor. This results in a resonant shunt, due to the capacitive nature of the piezoelectric device, thus constituting an electrical analogue of a DVA. Later, electromagnetic shunts were developed using electromagnetic transducers [18]. Because of the inductive nature of the electromagnetic transducer, a capacitor and a resistor are connected in parallel to form a resonant shunt in a manner analogous to the piezoelectric case. The optimal parameters of the shunt are then computed in order to perform an $H_\infty$-optimisation [19, 20, 21].

In previous works, an electromagnetic (EM) resonant shunt was proposed to enhance the performance of the DVA [22, 23]. In these cases, the transducer is placed in parallel to the DVA, between the frame and the primary structure, such that the analogous properties of the DVA and the resonant EM shunt are combined, resulting in stronger performance in term of resonance attenuation. The authors of [23] also tested placing the transducer between the primary structure and the DVA, but this configuration was not investigated further as it degrades the performance in term of resonance attenuation due to the emergence of an additional resonance. In the present work, this architecture is adopted with a resistive shunt instead of a resonant shunt. A similar architecture was previously investigated by [24] to enhance the damping of the DVA. However, the analysis was limited to a frequency range where the impedance associated with the transducer inductance is negligible. In this case, a resistive electromagnetic shunt connected between the primary structure and the DVA is strictly equivalent to introducing an additional viscous damping element into the DVA. Similar architectures with a piezoelectric shunt instead of an EM shunt were proposed in [25, 26], without thorough optimisations. Similar architectures have also been investigated for energy harvesting, with piezoelectric [27, 28] or EM [29, 30] transduction.

A range of alternatives has been examined with a view to compensating for the absence of damping in the DVA. As demonstrated in [31, 32], using eddy current is an effective method for adjusting the damping in the DVA. Moreover, nonlinear extensions of DVAs have received considerable attention since the 2000s thanks to the nonlinear Energy Sink (NES) concept. Its principle is to replace the linear spring of the DVA by an essentially nonlinear one. Originally proposed in [33], the concept received attention in a huge amount of works since then (more than three hundred selected publications are mentioned in the recent reviews [34, 35, 36]). Whereas most NES designs advantageously bring a robust adaptation to a frequency detuning and saturation phenomena, they may also be subjected to detached responses of large amplitude that negates their efficiency. One way of mitigating this issue is the use of a properly adjusted nonlinear damping, as theoretically shown in [37]. Even if this article focuses on adding electromagnetic damping to a (linear) DVA, it's extension to a NES may be of interest. Among other studies, the use of electromechanical shunts in NES applications was recently proposed: a piezoelectric NES in [38] and a mechanical NES enhanced with an electromagnetic resistive shunt for energy harvesting in [39].

In this context, this paper investigates the integration of an electromagnetic resistive shunt (R-shunt) in a mechanical DVA, with the aim of bringing a tunable and efficient source of damping. This may be used in the case of a purely elastic DVA (made of elastic springs, deformable elements, multibody systems such as pendulum...) to replace the standard damping source often brought by oil dampers or viscoelastic materials. The EM transducer is placed between the primary structure and the DVA and is short circuited by a resistor to form a resistive EM shunt. It is shown that it is able to bring damping, but that it is not fully equivalent to a simple dashpot since it brings an additional pole in the primary system's transfer function. An original optimisation is consequently necessary and based on a three fixed point strategy, similar to the standard optimisation procedure of a DVA based on two fixed points [2]. A similar frequency response, with three fixed points, is also observed for a DVA with a viscoelastic damping element [40]. It leads to optimise the DVA's tuning through its natural frequency, the R-shunt's electrical resistance and the electromechanical coupling factor of the transducer, leading to a dynamic response of the primary structure of almost the same shape than the one obtained with a standard mechanical optimised DVA. To the authors' knowledge, this DVA configuration involving an electromagnetic resistive shunt has not been previously explored, in particular beyond the frequency range in which the transducer's inductance can be neglected. It will be named a DVA+R-shunt absorber in the following.

Most studies optimise the absorber by analysing the displacement of the primary structure. However, acceleration analysis can offer valuable insights, particularly in relation to inertial effects. This work considers both displacement and acceleration as criteria for an $H_\infty$-optimisation. The same methodology could be extended to velocity, which also contributes to acoustic radiation [20], but is not considered in this article.

The paper is organised as follows. Section 2 introduces the system under study, composed of a primary structure coupled to a dynamic vibration absorber and an electromagnetic resistive shunt. The electromechanical model is formalised, and the three fixed points of the primary structure's frequency response function are identified. Section 3 focuses on optimising the displacement of the primary structure by performing an $H_\infty$-optimisation, based on the analysis of the fixed points. This leads to an optimal DVA's natural frequency, before testing two methods for optimising the R-shunt's resistance. Then, it is shown that the EM transducer's coupling factor must also be optimised. As this work is initially carried out under conservative mechanical conditions, the influence of a mechanical damping on both the primary structure and the DVA is analysed. In Section 4, the same methodology is applied to an $H_\infty$-optimisation of the acceleration response of the primary structure, leading to similar results. Finally, Section 5 presents the experimental validation of the absorber.

# 2 Modelling and fixed points

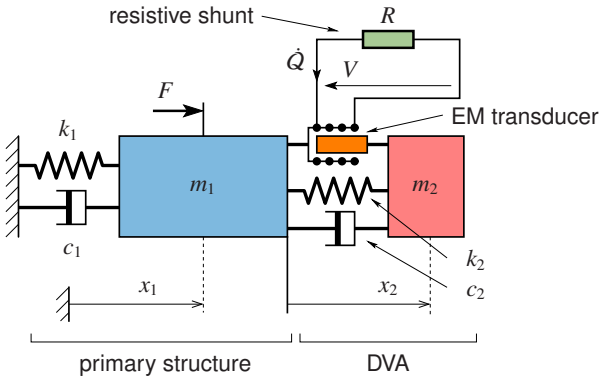



**Fig. 1:** Diagram of the primary structure coupled to the absorption device composed of a DVA and an electromagnetic resistive shunt between the two mechanical parts.

We consider in this article a primary structure that deforms under external loads and that is thus subjected to vibrations. Only one of its eigenmodes is considered, such that it is modelled by an equivalent mass / spring / dashpot system of constants $m_1$, $k_1$ and $c_1$ (see Fig. 1). Its oscillations are measured by displacement $x_1(t)$ (with $t$ the time) with respect to the ground and it is subjected to a force $F(t)$. Its vibrations are coupled to a dynamic vibration absorber (DVA), composed of a mass $m_2$, a stiffness $k_2$ and a viscous damper $c_2$, whose relative displacement with respect to the primary structure is denoted by $x_2(t)$. Then, the oscillations of the DVA are coupled to a resistive electromagnetic shunt (R-shunt), composed of an EM transducer in between the two mechanical structures, with its terminals connected to an electrical resistor of resistance $R$. In practice, this device may be constituted of a coil that is free to move in the radial magnetic field created by a permanent magnet.

## 2.1 Governing Equations

The EM transducer ensures an electromechanical conversion, producing a force $F_\mathrm{t} = \phi_\mathrm{t}\dot{Q}$ on $m_2$, where $\dot{Q}$ is the current flowing in the coil of the transducer ($Q$ is the electrical charge) and $\phi_\mathrm{t}$ is the force factor of the transducer. From an electrical perspective, the transducer can be modelled as an inductance $L_\mathrm{t}$, due to its inductive nature, in series with an electromotive force proportional to the relative velocity of the coil and the magnet. In our model, the internal resistance of the coil is included in the shunt resistance, such that $R$ is the sum of the internal resistance of the transducer and the additional resistance placed at its terminals. In order to maintain the passivity of the shunt, the global resistance is always positive $R > 0$, even if the resistance at the terminal of the transducer is negative, as will be done during the experiment in Section 5. Consequently, the voltage $V(t)$ at the terminals of the transducer is:

$$V = \phi_\mathrm{t}\dot{x}_2 - L_\mathrm{t}\ddot{Q} = R\dot{Q}. \tag{1}$$

As a consequence, the governing equations of the system, obtained using Lagrange's equations are:

$$\begin{cases} (m_1+m_2)\ddot{x}_1 + m_2\ddot{x}_2 + c_1\dot{x}_1 + k_1 x_1 = F & \text{(2a)} \\ m_2\ddot{x}_2 + m_2\ddot{x}_1 + c_2\dot{x}_2 + k_2 x_2 + \phi_\mathrm{t}\dot{Q} = 0 & \text{(2b)} \\ L_\mathrm{t}\ddot{Q} + R\dot{Q} - \phi_\mathrm{t}\dot{x}_2 = 0. & \text{(2c)} \end{cases}$$

It should be noted that the transducer's force factor $\phi_\mathrm{t}$ is considered the same for both electromotive and mechanical forces since we neglect ferromagnetic losses.

By dividing Eqs. (2a-c) respectively by $m_1$, $m_2$ and $L_\mathrm{t}$, and using the following change variable on the electrical load:

$$Q = \sqrt{\frac{m_2}{L_\mathrm{t}}}Q, \tag{3}$$

one obtains:

$$\begin{cases} (1+\mu)\ddot{x}_1 + \mu\ddot{x}_2 + 2\xi_1\omega_1\dot{x}_1 + \omega_1^2 x_1 = F/m_1 & \text{(4a)} \\ \ddot{x}_2 + \ddot{x}_1 + 2\xi_2\omega_2\dot{x}_2 + \omega_2^2 x_2 + \kappa\omega_1\dot{Q} = 0 & \text{(4b)} \\ \ddot{Q} + \dot{Q}/\tau_\mathrm{e} - \kappa\omega_1\dot{x}_2 = 0, & \text{(4c)} \end{cases}$$

where the following parameters are introduced:

$$\mu = \frac{m_2}{m_1}, \quad \omega_1 = \sqrt{\frac{k_1}{m_1}}, \quad \xi_1 = \frac{c_1}{2\sqrt{k_1 m_1}}, \quad \omega_2 = \sqrt{\frac{k_2}{m_2}}, \quad \xi_2 = \frac{c_2}{2\sqrt{k_2 m_2}}, \quad \tau_\mathrm{e} = \frac{L_\mathrm{t}}{R}, \quad \kappa = \frac{\phi_\mathrm{t}}{\omega_1\sqrt{m_2 L_\mathrm{t}}}. \tag{5}$$

Parameter $\mu$ represents the mass ratio of the DVA and the primary structure, $(\omega_1, \xi_1)$ denote the natural frequency and damping ratio of the naked primary structure (without absorber), whereas $(\omega_2, \xi_2)$ are those of the clamped DVA (with $x_1(t) = 0$) with the transducer in open-circuit ($\dot{Q}(t) = 0$). Parameter $\tau_\mathrm{e}$ is the electrical time constant of the electric circuit. The change of variable of Eq. (3) was chosen to make appear the same coupling coefficient $\kappa\omega_1$ in both Eqs. (4b,c). $\kappa$ is the dimensionless electromechanical coupling factor (EMCF). It can be obtained as a function of the natural electrical frequency of the DVA and the primary structure. Indeed, if the circuit is shorted ($V = 0$ or $\tau_\mathrm{e} \to \infty$), integrating Eq. (4c) once and eliminating $\dot{Q}$ between the result and Eq. (4b) shows that the natural frequency of the clamped DVA with the EM transducer in short-circuit is:

$$\check{\omega}_2 = \sqrt{\omega_2^2 + \kappa^2\omega_1^2}. \tag{6}$$

As a consequence, the EMCF reads:

$$\kappa = \sqrt{\frac{\check{\omega}_2^2 - \omega_2^2}{\omega_1^2}}. \tag{7}$$

One may notice that the EMCF is here defined with respect to $\omega_1$ instead of $\omega_2$ as it is often done in EM shunts applications (see [23]) or, analogously, for piezoelectric shunts (see *e.g* [19, 41]). This is a deliberate choice of the authors, to make independent the optimisation of the EM shunt from the one of the DVA in the next sections, such that $\kappa$ is independent of $\omega_2$. Moreover, on the contrary to piezoelectric shunts for which both open- and short-circuit natural frequencies are easily estimated experimentally, it is not the same for $\check{\omega}_2$ because of the internal resistance of the EM shunt, that makes the short-circuited transducer to be far from being conservative. This point will be addressed in Section 5.

It is also then convenient to define:

$$\omega_{1,\infty} = \frac{\omega_1}{\sqrt{1+\mu}}, \tag{8}$$

which is the natural frequency of the primary structure with the DVA locked to it (either $\dot{x}_2(t) = 0$, $c_2 \to +\infty$ or $k_2 \to +\infty$).

In all the subsequent analyses, the oscillations of the structure will be considered in the steady state, under harmonic excitation $F(t) = F_0\cos(\Omega t)$ at frequency $\Omega$. The Fourier transforms are denoted with a hat ($\hat{x}(\Omega)$ is a Fourier transform of $x(t)$) while $j = \sqrt{-1}$.

Considering Eqs. (4a-c) in the frequency domain leads to write the displacement of the primary structure as:

$$\hat{x}_1(\Omega) = \frac{F_0}{m_1} \frac{A(\Omega) + j\Omega\tau_e B(\Omega)}{C(\Omega) + j\Omega\tau_e D(\Omega)}, \tag{9}$$

where:

$$A(\Omega) = \omega_2^2 - \Omega^2 + 2j\xi_2\omega_2\Omega, \tag{10a}$$
$$B(\Omega) = \breve{\omega}_2^2 - \Omega^2 + 2j\xi_2\omega_2\Omega, \tag{10b}$$
$$C(\Omega) = \left[\omega_1^2 - (1+\mu)\Omega^2 + 2j\xi_1\omega_1\Omega\right](\omega_2^2 - \Omega^2 + 2j\xi_2\omega_2\Omega) - \mu\Omega^4, \tag{10c}$$
$$D(\Omega) = \left[\omega_1^2 - (1+\mu)\Omega^2 + 2j\xi_1\omega_1\Omega\right](\breve{\omega}_2^2 - \Omega^2 + 2j\xi_2\omega_2\Omega) - \mu\Omega^4, \tag{10d}$$

leading to define:

$$H_1(\Omega) = \hat{x}_1(\Omega)/\hat{x}_1(\Omega = 0), \tag{11}$$

the dimensionless frequency response function of the displacement of the primary structure.

## 2.2 Limit behaviours

From Eqs. (4a-c), one can analyse the limit behaviour of the R-shunt in the high- and low-frequency vibratory regimes, or, equivalently, for high and low values of $\tau_e$.

Considering Eq. (4c) in the frequency domain, $(-\Omega^2 + j\Omega\tau_e^{-1})\hat{Q} - j\Omega\kappa\omega_1\hat{x}_2 = 0$, one observes that at low frequencies, if $\Omega \ll \tau_e^{-1}$ (or for low values of $\tau_e$), the first term in Eq. (4c) can be neglected. In this case, the shunted transducer behaves as an additional viscous damper for the DVA, since $\dot{Q}$ can be eliminated in Eq. (4b) using Eq. (4c) to obtain:

$$\ddot{x}_2 + \ddot{x}_1 + (2\xi_2\omega_2 + \tau_e\kappa^2\omega_1^2)\dot{x}_2 + \omega_2^2 x_2 = 0. \tag{12}$$

On the contrary, at high frequencies (or for high values of $\tau_e$), $\Omega \gg \tau_e^{-1}$, the second term in Eq. (4c) can be neglected and the shunted transducer behaves as an additional stiffness for the DVA, since Eq. (4b) becomes:

$$\ddot{x}_2 + \ddot{x}_1 + 2\xi_2\omega_2\dot{x}_2 + \breve{\omega}_2^2 x_2 = 0, \tag{13}$$

with $\breve{\omega}_2 > \omega_2$ as defined by Eq. (6). This case was already addressed above for the discussion about the short-circuit case.

However, the subsequent analyses and optimisation (see in particular Section 3.2) will show that for some range of parameters, interesting values of the electrical constant are such that $\tau_e \simeq \omega_1 \simeq \Omega$, such that the two above cases are not sufficient for our analysis. Interesting behaviours of our system are thus more complicated than that of a simple DVA. The next section will show that they are related to the appearance of an additional pole in the transfer function.

## 2.3 Fixed points

The objective of this work is to optimise the absorber (DVA + R-shunt) in order to minimise the maximum amplitude of the frequency response function (FRF) of the primary structure expressed in Eq. (11), which is usually called an $H_\infty$-optimisation. In the case of a classical DVA, a robust parameter selection method is often proposed by considering the primary structure as conservative ($\xi_1 = 0$). The FRF of the primary system then shows two fixed points when the damping ratio of the DVA is varied [2]. Then, the DVA natural frequency is selected such that the amplitudes of the fixed points are equal, while the damping ratio is chosen to make the tangents at these points as horizontal as possible [42].

In the present study, the aim is to optimise the system such that the R-shunt is a tunable and efficient source of damping in the DVA, replacing standard damping sources (oil damper or viscoelastic material). As a consequence, we consider here, as a preliminary, that the primary structure and the DVA are conservative: $\xi_1 = \xi_2 = 0$. In this case, Eq. (11) simplifies to:

$$H_1(\Omega) = \omega_1^2 \frac{\omega_2^2 - \Omega^2 + j\Omega\tau_e(\omega_2^2 + \kappa^2\omega_1^2 - \Omega^2)}{(\omega_1^2 - (1+\mu)\Omega^2)(\omega_2^2 - \Omega^2) - \mu\Omega^4 + j\Omega\tau_e[(\omega_1^2 - (1+\mu)\Omega^2)(\omega_2^2 + \kappa^2\omega_1^2 - \Omega^2) - \mu\Omega^4]}. \tag{14}$$

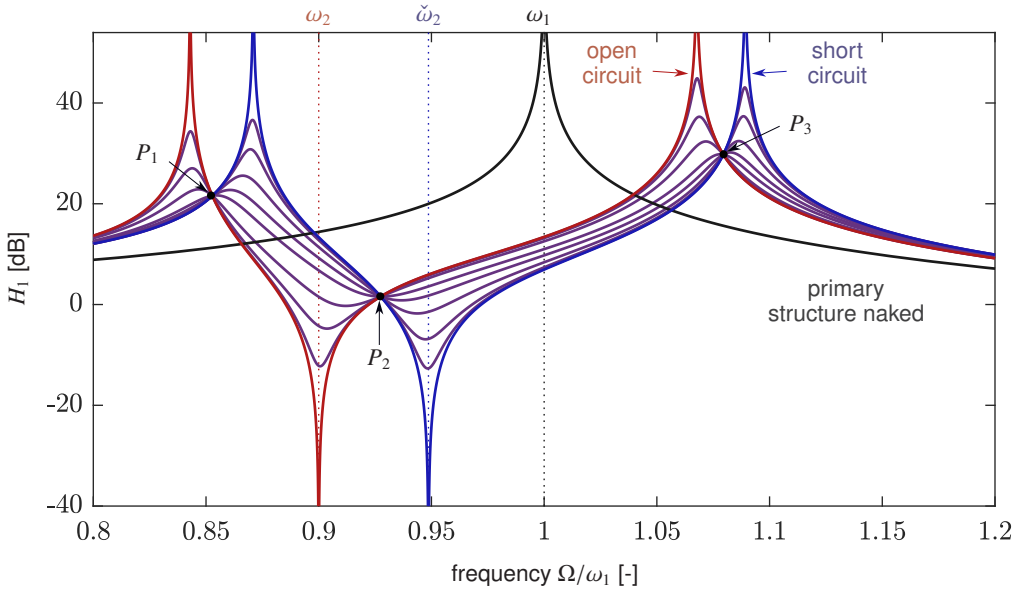



**Fig. 2:** Modulus of $H_1(\Omega)$ for $\xi_1 = \xi_2 = 0$ under several conditions. (black curve): uncoupled primary structure (without DVA and EM-shunt); (red curve): transducer in open circuit ($\tau_e = 0$); (blue curve): transducer in short circuit ($\tau_e = +\infty$); (purple curves): eight values of $\tau_e \in [0, +\infty]$. The parameters are $\omega_2 = 0.9\omega_1$, $\mu = 0.05$ and $\kappa = 0.3$. The dashed vertical curves indicates the extrema of the frequency response while points $P_1$, $P_2$ and $P_3$ denote the fixed points.

Figure 2 presents the modulus of $H_1(\Omega)$ of the previous equation, in the particular case $\omega_2 = 0.9\omega_1$, for various values of the parameters. First, the black plot shows the case of a naked primary structure (without any absorber, $\mu = 0$), for which its resonance at $\Omega = \omega_1$ is clearly visible. The red and blue plots represent the cases where the transducer is respectively in open circuit ($\tau_e = 0$) and short circuit ($\tau_e \to +\infty$). In both cases, one observes that the absorber creates an antiresonance at its natural frequency, at $\Omega = \omega_2$ or $\Omega = \breve{\omega}_2$, consistently with Eq. (6). It also adds a new pole in the transfer function, such that the single resonance at $\omega_1$ is replaced by two resonances on either side of the antiresonance. Finally, several purple plots show cases with several finite values of $\tau_e$, adding dissipation in the system. One can see that the resonances and the antiresonance are weakened and that sweeping $\tau_e$ from 0 to $+\infty$ leads to pass continuously from the short- to the open-circuit (conservative) cases. Nevertheless, a remarkable result appears: there are *three fixed points* in the transfer function when $\tau_e$ is varied, named $P_1$, $P_2$ and $P_3$ in Fig. 2. An analogous result has already been found in the case of a viscoelastic DVA in [40].

The frequency of the independent fixed points can be determined by equating the modulus of $H_1(\Omega)$ in the two extreme cases of $\tau_e = 0$ and $\tau_e \to \infty$ leading to:

$$\frac{A(\Omega)}{C(\Omega)} = \pm\frac{B(\Omega)}{D(\Omega)}, \tag{15}$$

in the particular case $\xi_1 = \xi_2 = 0$. The case $AD = BC$ leads to the trivial solution $\Omega^2 = 0$, whereas the case $AD = -BC$ leads to the following third order polynomial equation in $X = \Omega^2$:

$$P(X) = 2X^3 - \left[(2+\mu)(\omega_2^2 + \breve{\omega}_2^2) + 2\omega_1^2\right]X^2 + 2\left[(\omega_2^2 + \breve{\omega}_2^2)\omega_1^2 + (1+\mu)\omega_2^2\breve{\omega}_2^2\right]X - 2\omega_2^2\breve{\omega}_2^2\omega_1^2 = 0, \tag{16}$$

whose solutions are the frequencies of the fixed points.

The sign of the above polynomial $P(X)$ is computed at the special frequencies successively:

$$P(0) < 0, \quad P(\omega_2^2) > 0, \quad P(\breve{\omega}_2^2) < 0, \quad P(+\infty) > 0. \tag{17}$$

The signs alternate between consecutive evaluations. Since the polynomial is continuous, by the intermediate value theorem, its roots must lie in the intervals where the sign changes. Consequently, there are three fixed points:

$$\Omega_{P_1} \in [0,\, \omega_2], \quad \Omega_{P_2} \in [\omega_2,\, \breve{\omega}_2], \quad \text{and} \quad \Omega_{P_3} \in [\breve{\omega}_2,\, +\infty], \tag{18}$$

where $\Omega_{P_1}$, $\Omega_{P_2}$, and $\Omega_{P_3}$ are the frequencies corresponding to the fixed points $P_1$, $P_2$, and $P_3$, respectively. In the following, they are numerically computed by a classical polynomial roots computation algorithm.

### 2.4 Frequency scaling

By defining a dimensionless time $\bar{t} = \omega_1 t$ scaled by $\omega_1$, the governing equations (4a-c) can be rewritten as:

$$\begin{cases} (1+\mu)\ddot{x}_1 + \mu\ddot{x}_2 + 2\xi_1\dot{x}_1 + x_1 = F/k_1 & \text{(19a)} \\ \ddot{x}_2 + \ddot{x}_1 + 2\xi_2\bar{\omega}_2\dot{x}_2 + \bar{\omega}_2^2 x_2 + \kappa\dot{Q} = 0 & \text{(19b)} \\ \ddot{Q} + \dot{Q}/\bar{\tau}_\mathrm{e} - \kappa\dot{x}_2 = 0, & \text{(19c)} \end{cases}$$

where $\bar{\omega}_2 = \omega_2/\omega_1$ and $\bar{\tau}_\mathrm{e} = \tau_\mathrm{e}\omega_1$ are dimensionless frequency and time constant. As a consequence, one can see that the optimisation problem *is independent of* $\omega_1$. However, to keep the symmetry in the equations between $\omega_1$ and $\omega_2$ and for the sake of clarity, $\omega_1$ is kept in the equations in the following.

## 3 Absorber optimisation to reduce the displacement of the primary structure

The goal of this section is to optimise the R-shunt / DVA parameters ($\omega_2$, $\tau_\mathrm{e}$ and $\kappa$) in order to perform an $H_\infty$-optimisation on the displacement of the primary structure. This optimisation is performed in four sequential steps. (i) The optimum natural frequency $\omega_2$ of the DVA is found by equalising the amplitude of the external fixed points $P_1$ and $P_3$; (ii) the optimum electrical time constant $\tau_\mathrm{e}$ is found by minimising the maximum amplitude of $|H_1(\Omega)|$; (iii) the system is further optimised by finding optimum values of the EMCF $\kappa$, that influences the relative amplitude of the three fixed points. Finally, (iv) the previous optimisation is validated and extended thanks to a fully numerical procedure. All those optimisations are done as a function of the mass parameter $\mu$.

### 3.1 Optimisation of the natural frequency $\omega_2$ of the DVA

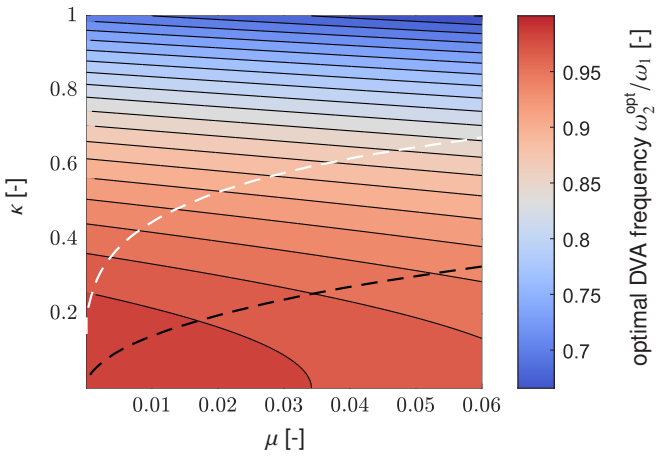



**Fig. 3:** Evolution of $\omega_2^{\mathrm{opt}}/\omega_1$ as a function of $\mu$ and $\kappa$. The black dashed curve shows the threshold value below which $\omega_2^{\mathrm{opt}}$ exceeds the classical optimal value for a DVA $\omega_{\mathrm{dva}}$ (Eq. (21)). The white dashed curve marks the threshold above which the amplitude of the central fixed point $P_2$ is higher than that of $P_1$ and $P_3$.

Analogously to the case of a standard DVA (without an R-shunt), if the natural frequency of the DVA $\omega_2$ varies, the relative amplitude of the two external fixed point ($P_1$ and $P_3$ on Fig. 2) changes. The aim of this section is to determine the value $\omega_2^{\mathrm{opt}}$ of $\omega_2$ which allows $P_1$ and $P_3$ to be at the same amplitude in the mechanical conservative case ($\xi_1 = \xi_2 = 0$). This condition can be expressed as:

$$|H_1(\Omega_{P_1})| = |H_1(\Omega_{P_3})|, \tag{20}$$

where $\Omega_{P_1}$ and $\Omega_{P_3}$ are the frequencies of $P_1$ and $P_3$, obtained numerically as the two extremal positive solutions of Eq. (16). Following the time scaling of Section 2.4 and Eq. (16), $\omega_2^{\mathrm{opt}}/\omega_1$ is a function of $\mu$ and $\kappa$ only.

Consequently, $\omega_2^{\mathrm{opt}}/\omega_1$ is computed numerically for a selection of values of $(\mu, \kappa)$ within the domain $([0.001, 0.060], [0.001, 1.000])$, by (i) computing $(\Omega_{P_1}, \Omega_{P_3})$ with the roots of (16) and (ii) optimising the value of $\omega_2$ to ensure Eq. (20). In practice, a

simplex search method (function `fminsearch` of Matlab) is used. The result is shown as a contour plot in Fig. 3. In addition, the black dashed curve in Fig. 3 indicates the threshold above which the optimum natural frequency of the absorber $\omega_2^{\text{opt}}$ is smaller than that of a classical DVA, whose relation is recalled here:

$$\omega_{\text{dva}} = \frac{\omega_1}{1+\mu}. \tag{21}$$

It can be seen that increasing $\mu$ decreases $\omega_2^{\text{opt}}$, in the same way as a classical DVA. Similarly, increasing $\kappa$ decreases $\omega_2^{\text{opt}}$. Consequently, one observes that the presence of the R-shunt changes the tuning of the DVA, that has to be over- or under-tuned, depending on the value of the EMCF $\kappa$ and the mass ratio $\mu$.

The white dashed curve marks the threshold above which the pair $(\mu, \kappa)$ and the optimal value $\omega_2^{\text{opt}}$ makes the amplitude of the central fixed point $P_2$ higher than the amplitude of the two external fixed point ($P_1$ and $P_3$). This point will be examined in the upcoming sections.

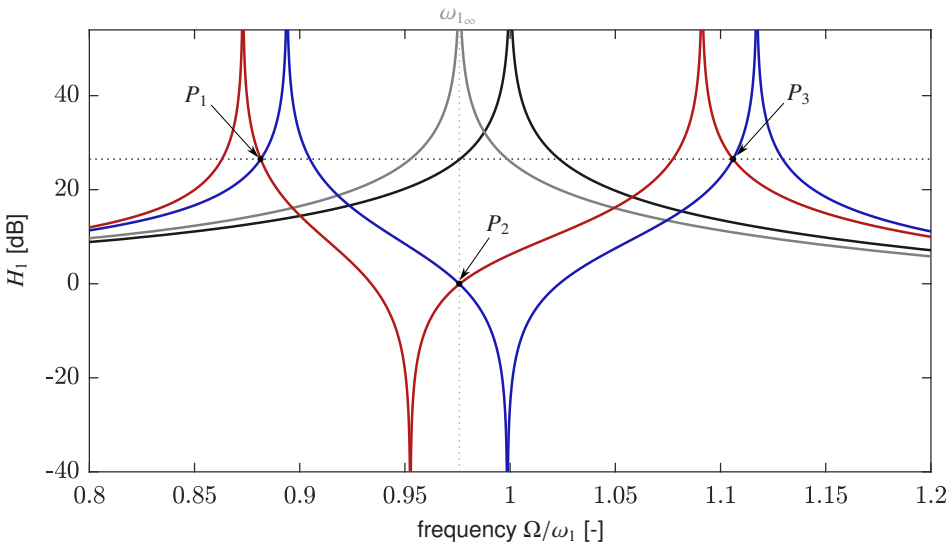



**Fig. 4:** Modulus of $H_1(\Omega)$ with $\xi_1 = \xi_2 = 0$ and $\omega_2 = \omega_2^{\text{opt}}$ under several conditions. (black curve): uncoupled primary structure (without DVA and EM-shunt); (grey curve) locked DVA (with $k_2 \to +\infty$ or $c_2 \to +\infty$); (red curve): transducer in open circuit ($\tau_{\text{e}} = 0$); (blue curve): transducer in short circuit ($\tau_{\text{e}} = +\infty$). The parameters are $\mu = 0.05$ and $\kappa = 0.3$.

Figure 4 presents severals FRF of the primary structure, for a given value of $(\mu, \kappa)$, with $\omega_2 = \omega_2^{\text{opt}}$, such that the amplitude of the two external fixed points is equal. As illustrated in this figure (and graphically verified for other values of $(\mu, \kappa)$), the natural frequency $\omega_{1,\infty}$ (see Eq. (8)) of the structure with the locked DVA matches exactly the frequency of the central fixed point $P_2$:

$$\Omega_{P_2} = \omega_{1,\infty}. \tag{22}$$

Then, since $\Omega_{P_2}$ is a solution of Eq. (16), prescribing $\Omega = \Omega_{P_2} = \omega_{1,\infty} = \omega_1/\sqrt{1+\mu}$ in this equation shows after a few analytical developments that the optimum natural frequency $\omega_2 = \omega_2^{\text{opt}}$ naturally reads:

$$\omega_2^{\text{opt}} = \omega_1 \sqrt{\frac{1}{1+\mu} - \frac{\kappa^2}{2}}. \tag{23}$$

It was numerically verified that this relationship exactly coincides with the numerical values of $\omega_2^{\text{opt}}$ shown in Fig. 3. This closed form expression of $\omega_2^{\text{opt}}$ is advantageous for the purpose of tuning the natural frequency of the present DVA coupled to an R-shunt.

Moreover, it is actually possible to derive this expression analytically, as suggested by one of the reviewers during the peer review process. The method is provided in Appendix A. It also allows the fixed-point frequencies to be determined in closed-from expressions, in the present case $\omega_2 = \omega_2^{\text{opt}}$.

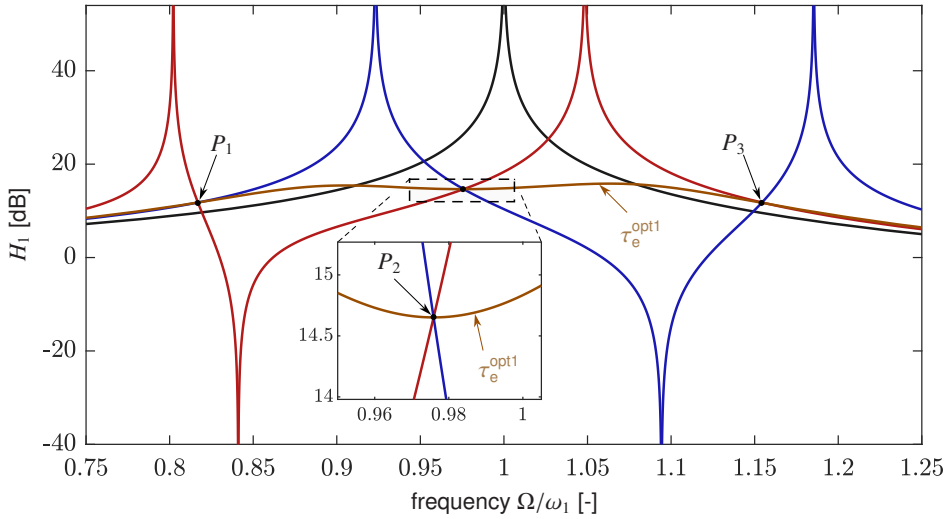



**Fig. 5:** Modulus of $H_1(\Omega)$ with $\xi_1 = \xi_2 = 0$ and $\omega_2 = \omega_2^{opt}$ under several conditions: (black curve): uncoupled primary structure; (red curve): transducer in open circuit ($\tau_e = 0$); (blue curve): transducer in short circuit ($\tau_e = +\infty$); (gold curve): shunt optimised as $\tau_e = \tau_e^{opt1}$. The parameter are $\mu = 0.05$ and $\kappa = 0.7$ in order to have the fixed point $P_2$ above the two others.

## 3.2 Optimisation of $\tau_e$ and $\kappa$

The optimum natural frequency of the DVA $\omega_2^{opt}$ has been established in the previous section (Eq. (23)) as a function of the mass ratio $\mu$ and the EMCF $\kappa$ of the transducer. The objective is now to find the optimal electrical time constant $\tau_e$. Two strategies are examined: the first is inspired by the standard optimisation strategy of DVAs of choosing the damping that allows an horizontal tangent at the fixed points; the second is based on a numerical minimisation algorithm.

### 3.2.1 First strategy to optimise $\tau_e$

Since for all values of $\tau_e$ the FRFs pass through the fixed points $P_1$, $P_2$ and $P_3$ (see Fig. 2), the first step is to place the two extremal ones, $P_1$ and $P_3$, at the same amplitude by choosing $\omega_2$ with Eq. (23). Then, depending on the values of $\mu$ and $\kappa$, the amplitude of the central fixed point $P_2$ may be lower or higher than that of the two others. Precisely, for values of $(\mu, \kappa)$ above the white dashed curve in Fig. 3, $|H_1(\Omega_{P_2})| > |H_1(\Omega_{P_1,P_3})|$. This leads to two optimisation cases.

Firstly, if $|H_1(\Omega_{P_2})| > |H_1(\Omega_{P_1,P_3})|$, we choose the optimal value of $\tau_e$ such that the tangent at $P_2$ is horizontal, to ensure that a maximum is reached at this point. In this case, solving:

$$\left.\frac{\partial |H_1(\Omega)|^2}{\partial \Omega^2}\right|_{\Omega=\Omega_{P_2}} = 0 \tag{24}$$

yields the optimal electrical time constant, denoted $\tau_e^{opt1}$. For this, the numerator of the derivative in Eq. (24) is symbolically obtained using the values of $A$, $B$, $C$, $D$ and their derivatives with respect to $X = \Omega^2$ (Eqs. (10a-d)), obtaining a second order polynomial in $\tau_e^2$. Then, $\Omega$ is replaced by $\Omega_{P_2}$ numerically evaluated with the second root of the polynomial in Eq. (16) and $\tau_e^{opt1}$ is obtained with the maximum root of the second order polynomial in $\tau_e^2$. An example of this case is presented in Fig. 5.

Otherwise, if the amplitude of the central fixed point $P_2$ is lower than that of the two others (*i.e.* for parameters $(\mu, \kappa)$ located below the black dashed curve in Fig. 3), the maxima of the FRF should occur at $\Omega_{P_1}$ and $\Omega_{P_3}$ for optimal vibration reduction. This requirement leads to the conditions:

$$\left.\frac{\partial |H_1(\Omega)|^2}{\partial \Omega^2}\right|_{\Omega=\Omega_{P_1}} = 0, \quad \left.\frac{\partial |H_1(\Omega)|^2}{\partial \Omega^2}\right|_{\Omega=\Omega_{P_2}} = 0, \tag{25}$$

which, however, cannot be satisfied simultaneously. Specifically, the solution of the first of Eqs. (25), denoted $\tau_e^{P_1}$, that enforces a zero slope at fixed point $P_1$, typically differs from the solution of the second equation, $\tau_e^{P_3}$, that enforces

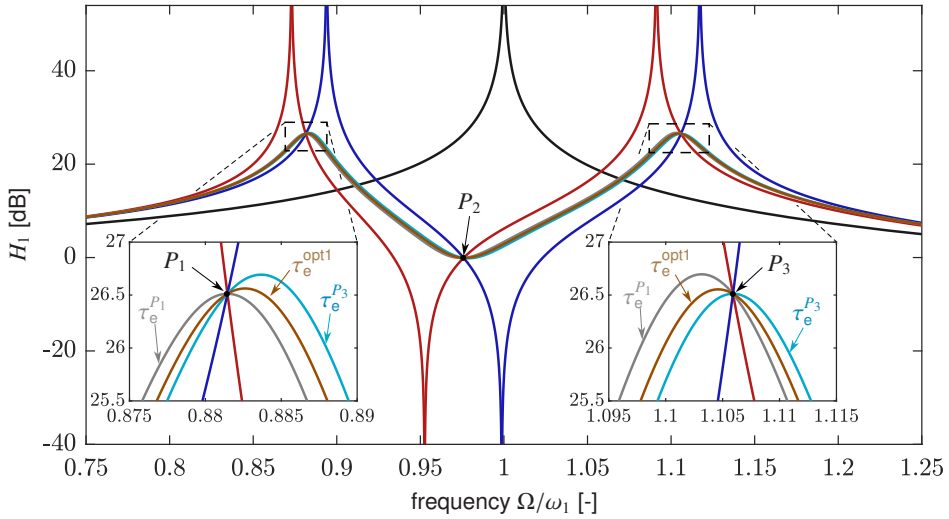



**Fig. 6:** Modulus of $H_1(\Omega)$ with $\xi_1 = \xi_2 = 0$ and $\omega_2 = \omega_2^{opt}$ under several conditions: (black curve): uncoupled primary structure; (red curve): transducer in open circuit ($\tau_e = 0$); (blue curve): transducer in short circuit ($\tau_e = +\infty$); (grey curve): shunt optimised as $\tau_e = \tau_e^{P_1}$; (light blue curve): shunt optimised as $\tau_e = \tau_e^{P_3}$; (gold curve): shunt optimised as $\tau_e = \tau_e^{opt1}$. The parameter of the DVA are $\mu = 0.05$ and $\kappa = 0.3$, to have the fixed point $P_2$ below the two others.

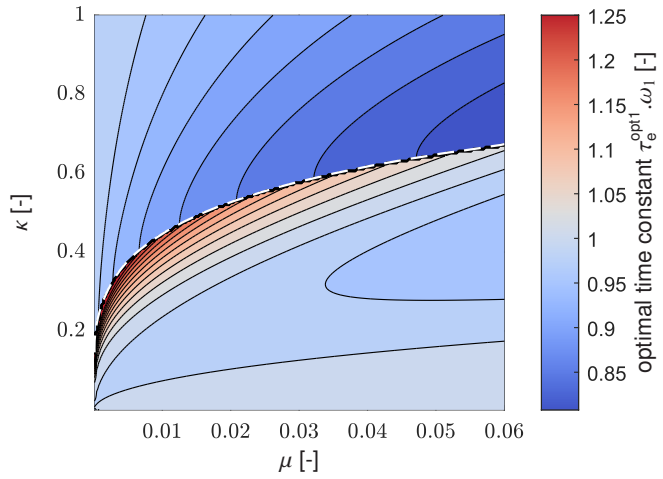



**Fig. 7:** Evolution of the time constant optimal value $\tau_e^{opt1}$, scaled by $\omega_1$, as a function of $(\mu, \kappa)$. The white dashed curve marks the threshold above which the amplitude of the central fixed point $P_2$ is higher than that of $P_1$ and $P_3$.

the same condition at fixed point $P_3$. To obtain a practical compromise, the optimal time constant is defined as the average of the two values:

$$\tau_e^{opt1} = \frac{\tau_e^{P_1} + \tau_e^{P_3}}{2}. \tag{26}$$

An example of this case is presented in Fig. 6. It is clearly observable that this value allows minimisation of the maximum of the FRF. The numerical values of $\tau_e^{P_1}$ and $\tau_e^{P_3}$ are determined with the same numerical strategy than for $\tau_e^{opt1}$ in the previous case where $P_2$ is above $P_1$ and $P_3$.

Figure 7 shows the values of $\tau_e^{opt1}$, scaled by $\omega_1$, as a function of the two independent parameters $(\mu, \kappa)$. The white dashed curve shows the threshold pair value of $(\mu, \kappa)$ for which the amplitude of the fixed point $P_2$ is higher than the two others ones. One can observe that for values of $(\mu, \kappa)$ below the threshold, the optimal time constant $\tau_e^{opt1}$ increases as the pair approaches the threshold and experiences a jump at the threshold crossing. This non-smooth evolution of $\tau_e^{opt1}$ led us to investigate a full numerical optimisation for $\tau_e$.

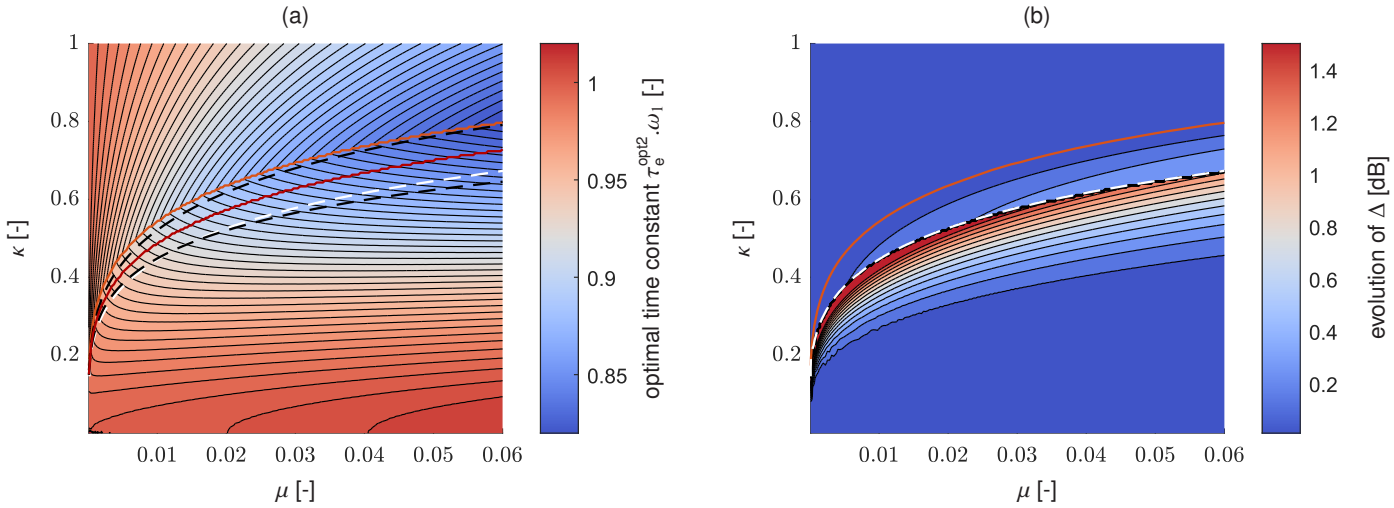



**Fig. 8:** (a) Evolution of the time constant optimal value $\tau_e^{opt2}$, scaled by $\omega_1$, as a function $(\mu, \kappa)$. The red curve shows the optimised value $\kappa_{opt0}$ of $\kappa$ as a function of $\mu$. The area between the two dashed black curve corresponds to values of $(\mu, \kappa)$ for which the DVA+R-shunt absorber has better performance than a standard mechanical DVA. (b) Evolution of $\Delta$ (see Eq. (27)) as a function of $(\mu, \kappa)$. In both plots, the orange curve limits the number of extrema of $|H_1(\Omega)|$: above, it has one maximum and below it has two maxima and one minimum. The white dashed curve marks the threshold above which the amplitude of the central fixed point $P_2$ is higher than that of $P_1$ and $P_3$.

### 3.2.2 Second strategy to optimise $\tau_e$

An alternative approach to determine the optimal value of the electrical time constant is to compute directly the value of $\tau_e$, called $\tau_e^{opt2}$, which minimises the maximum value of $|H_1|$, in the case of $\omega_2 = \omega_2^{opt}$. For a given $\tau_e$, the extrema of $|H_1|$ are first obtained by computing symbolically the roots of the derivative of $|H_1|^2$ with respect to $X = \Omega^2$, a seventh order polynomial in $X$ (see Eqs. (10a-d)), and keeping the real positive ones, leading to one or three values of $\Omega$ for the extrema. Then, $\tau_e^{opt2}$ is obtained with a simplex search method (the function `fminsearch` of Matlab) as the value of $\tau_e$ that minimises the maximum of $|H_1(\Omega)|$.

The contour plot diagram in Fig. 8(a) shows the results of this optimisation, the value of $\tau_e^{opt2}$ scaled by $\omega_1$, as a function of the independent variables $(\mu, \kappa)$. One observes that the global evolution of $\tau_e^{opt2}$ is smoother than the one of $\tau_e^{opt1}$ (compare Figs. 7 and 8(a)) since it is now a continuous function of $(\mu, \kappa)$. One can nevertheless observe a jump in the slope, indicated in Fig. 8(a) as the orange curve, that occurs because the number of maxima of the frequency response changes: below the orange curve, $|H_1(\Omega)|$ has two maxima and one minimum (at $\Omega = \Omega_{P_2}$, like in Figs. 5 or 6), whereas above the orange curve, $|H_1(\Omega)|$ has only one maximum at $\Omega = \Omega_{P_2}$. The white dashed curve of Fig. 7 is also shown and represents the threshold above which the amplitude at $P_2$ is larger than the ones at $P_1$ and $P_3$. It is observed that the two limits are distinct. This is illustrated in Fig. 5 that shows $|H_1(\Omega)|$ in a case in between the orange and white dashed curve and for which it is clear the two maxima of the frequency response are far from the two extremal fixed points $P_1$ and $P_3$.

The two optimal values $\tau_e^{opt1}$ and $\tau_e^{opt2}$ are compared in Fig. 8(b), that shows the relative difference between the maximum amplitude of the two associated FRFs, expressed in dB, defined as:

$$\Delta = 20 \log_{10} \frac{\max_{\Omega} |H_1(\Omega)|_{\tau_e = \tau_e^{opt1}}}{\max_{\Omega} |H_1(\Omega)|_{\tau_e = \tau_e^{opt2}}}. \tag{27}$$

The two limits (orange curve and dashed white curve) of Figs. 7 and 8(a) are reported on this plot. One can observe that $\Delta$ is always positive, indicating that the second strategy is more efficient than the first one, especially in the region close to the white dashed curve where $\tau_e^{opt1}$ is the highest (see Fig. 7), showing that the first strategy overestimate the optimal value of $\tau_e$. This is further illustrated in Fig. 9 in which the two optimisation strategies for $\tau_e$ are compared, in a case for which the fixed point $P_2$ exhibits a higher amplitude than the fixed points $P_1$ and $P_3$ (same case as Fig. 5). One can observe that the second optimisation (orange curve) leads to a more symmetric response than the first (golden curve), with a maximum slightly below, as expected. In the remainder of the study, the optimisation of $\tau_e$ will be carried out using the second strategy.

Figure 10 shows an example of optimised FRF (in orange) obtained for a given pair $(\mu, \kappa)$, with the absorber

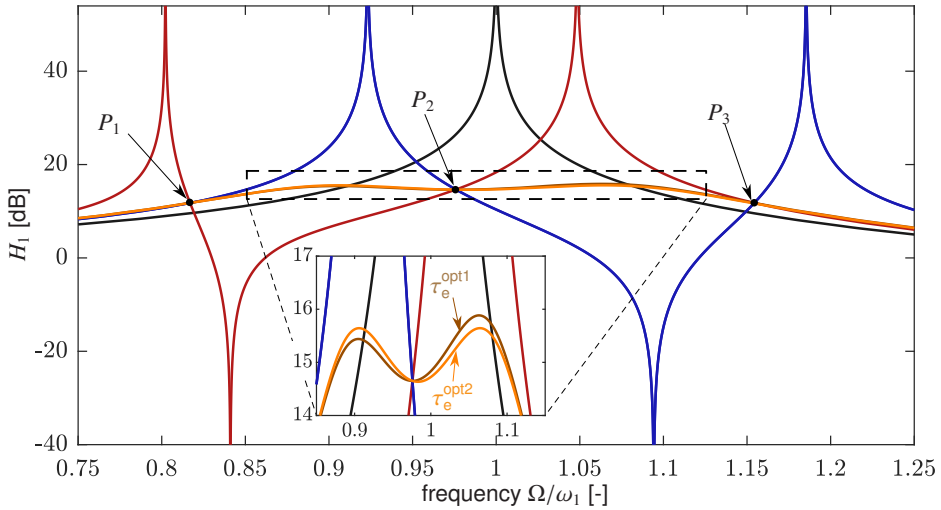



**Fig. 9:** Modulus of $H_1(\Omega)$ with $\xi_1 = \xi_2 = 0$ and $\omega_2 = \omega_2^{opt}$ under several conditions: (black curve): uncoupled primary structure; (red curve): transducer in open circuit ($\tau_e = 0$); (blue curve): transducer in short circuit ($\tau_e = +\infty$); (gold curve): shunt optimised as $\tau_e = \tau_e^{opt1}$; (orange curve): shunt optimised as $\tau_e = \tau_e^{opt2}$. The parameter are $\mu = 0.05$ and $\kappa = 0.7$ in order to have the fixed point $P_2$ above the two others.

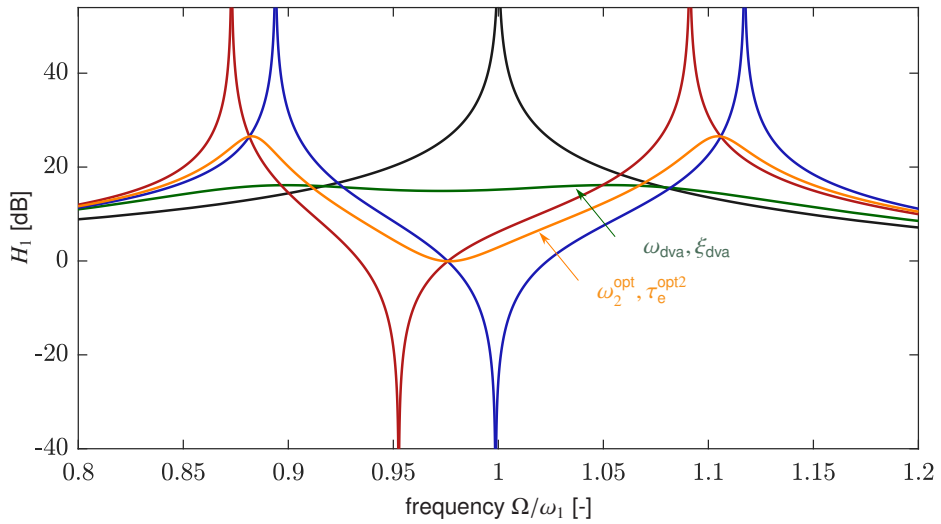



**Fig. 10:** Modulus of $H_1(\Omega)$ with $\xi_1 = \xi_2 = 0$ and $\omega_2 = \omega_2^{opt}$ under several conditions. (black curve): uncoupled primary structure (without DVA and EM-shunt); (red curve): transducer in open circuit ($\tau_e = 0$); (blue curve): transducer in short circuit ($\tau_e = +\infty$); (orange curve): $\tau_e = \tau_e^{opt2} = 0.9665/\omega_1$. (green dashed curve) optimised DVA without EM shunt (its parameters follow Eqs. (21) and (28)). The parameters are $\mu = 0.05$ and $\kappa = 0.3$.

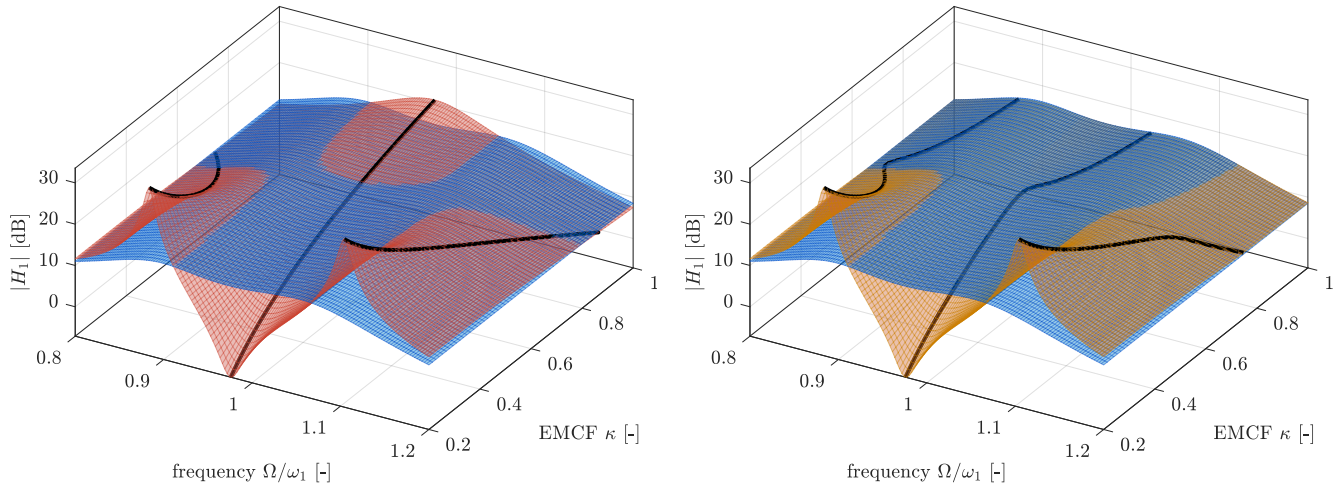



**Fig. 11:** Variation of the modulus of $H_1(\Omega)$ as a function of the EMCF $\kappa$. The red surface is the case of a DVA + R-shunt absorber, for $\xi_2 = 0$ and for optimal values of the parameters $\omega_2 = \omega_2^{\text{opt}}$ and $\tau_e = \tau_e^{\text{opt2}}$; the orange surface is the same for optimal values $\omega_2 = \omega_2^*$ and $\tau_e = \tau_e^*$. The blue surface is the case of an optimal DVA with $\omega_2 = \omega_{\text{dva}}$ and $\xi_2 = \xi_{\text{dva}}$. In both cases, $\xi_1 = 0$ and the mass ratio is $\mu = 0.05$. The black solid curves are the locus of the fixed points.

parameters chosen as $\omega_2 = \omega_2^{\text{opt}}$ and $\tau_e = \tau_e^{\text{opt2}}$. The FRF appears optimal, but since it passes through the fixed points, it leads in this case to a response which has a higher amplitude than the one that would be obtained with a DVA without an R-shunt, but with optimised stiffness and damping. The latter is shown in green, with the DVA's natural frequency $\omega_2$ that follows Eq. (21) and its damping ratio $\xi_2$ equal to [42]:

$$\xi_{\text{dva}} = \sqrt{\frac{3\mu}{8(1+\mu)}}. \tag{28}$$

As shown in the next section, this situation can be improved by optimising the EMCF $\kappa$, yielding to slightly more effective reduction than an optimally tuned DVA.

### 3.2.3 Optimisation of $\kappa$

As enlightened in the previous section, when the EMCF $\kappa$ is varied for a given value of the mass ratio $\mu$ and with the absorber parameters at their optimal value ($\omega_2 = \omega_2^{\text{opt}}$, $\tau_e = \tau_e^{\text{opt2}}$), one observes that the amplitude of $H_1(\Omega)$ at the fixed points varies, as well as its number of extrema. This is illustrated in Fig. 11, for which the corresponding red surface has three extrema for low values of $\kappa$ and only one for high values. Observing the black curves, which show the locus of the three fixed points, also show that when $\kappa$ increases, the amplitude at the two extremal fixed points $P_1$ and $P_3$ decreases, whereas the amplitude at the central one $P_2$ increases. This trend is confirmed by computing the amplitude at the fixed point $P_2$ as a function of $\kappa$, that reads:

$$H_1(\Omega_{P_2}) = \frac{\kappa^2(1+\mu)^2}{2\mu}, \tag{29}$$

established by using Eqs (22), (23) in (14) with $\tau_e = 0$. Figure 11 also shows the frequency response of the primary system with an optimally tuned DVA (without R-shunt), represented by the blue surface. One observes that for a narrow interval of values of $\kappa$ (denoted as $[\kappa_{\text{opt1}}, \kappa_{\text{opt2}}]$ in the following), the red surface is below the blue surface, such that the performance of the DVA+R-shunt absorber is better than a standard mechanical DVA. As a consequence, it is of interest of optimising also the EMCF to obtain a powerful absorber.

Figure 12 illustrates further the role of the parameter $\kappa$ in the performance of the device, for a fixed value of $\mu$. The blue curve in Fig. 12(a) shows the difference between the frequency responses of the optimised DVA+R-shunt absorber (with $\omega_2 = \omega_2^{\text{opt}}$, $\tau_e = \tau_e^{\text{opt}}$, $\xi_2 = 0$) and that of a classical optimised DVA ($\omega_2 = \omega_{\text{dva}}$, $\xi_2 = \xi_{\text{dva}}$), as a function of $\kappa$. It shows a minimum, the corresponding value of $\kappa$ being considered optimal and denoted $\kappa_{\text{opt0}}$, for a given $\mu$. In

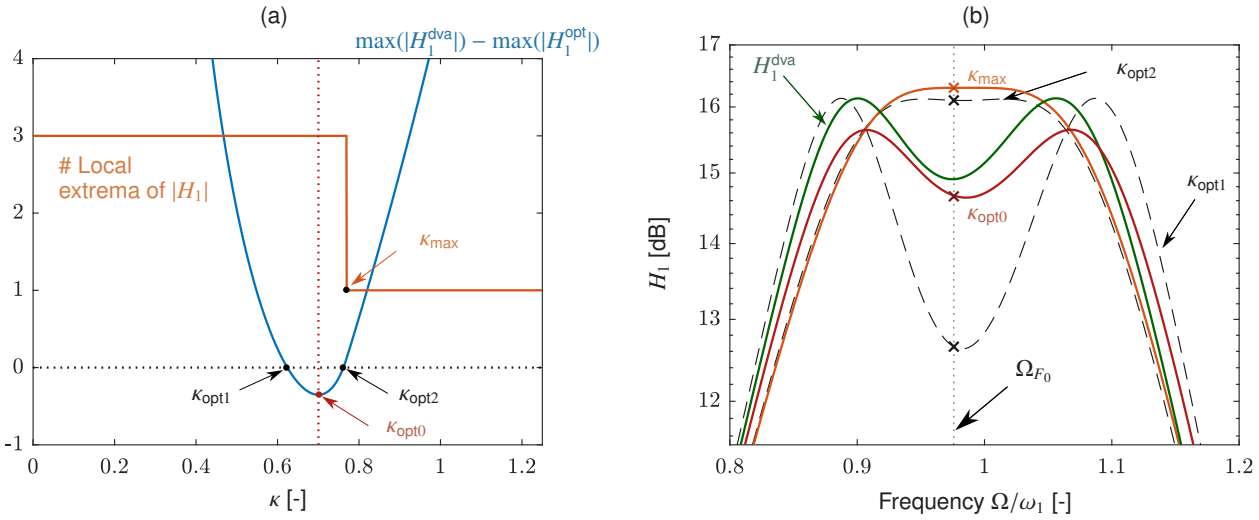



**Fig. 12:** Remarkable values of $\kappa$ for $\mu = 0.05$. (a) The sky-blue curve shows the difference between the maximum modulus of $H_1$ of the optimised device and that of the optimised DVA. The interval $[\kappa_{opt1}, \kappa_{opt2}]$ indicates the range of $\kappa$ where the maximum modulus of $H_1$ of the device is lower than the maximum FRF of the optimised DVA. The minimum of the sky-blue curve corresponds to $\kappa^{opt}$. The orange curve shows the number of stationary points of the FRF of the optimised device. The change in the number of stationary points occurs at $\kappa_{max}$.(b) FRFs for different values of $\kappa$ with their corresponding optimised parameters $(\omega_2^{opt}, \tau_e^{opt})$. The green curve shows the modulus of $H_1$ for an optimised DVA.

other words, regardless of the DVA mass ratio, there is always an optimal transducer capable of minimising $|H_1(\Omega)|$. The corresponding frequency response is plotted in dark red in Fig. 12(b) and the value of $\kappa_{opt0}$ as a function of $\mu$ is shown in Fig. 8(a).

Around $\kappa_{opt0}$, in the interval $[\kappa_{opt1}, \kappa_{opt2}]$, the DVA+R-shunt absorber remains more efficient than an optimised DVA. This interval, highlighted in Fig. 8(a), widens as $\mu$ increases. The frequency response $|H_1(\Omega)|$ corresponding to those limit values is shown in dashed black, as an illustration, in Fig. 12(b). This figure also shows in orange the frequency response for $\kappa = \kappa_{max}$, the particular value of $\kappa$ that corresponds to the orange curve in Figs. 8(a,b), above which $|H_1(\Omega)|$ has only one maximum.

### 3.2.4 Numerical optimisation beyond the fixed point method

The optimisations carried out in the previous subsections are based on choosing $\omega_2$ such that the FRF amplitudes at the two external fixed points are equal (see Eq. (20)). It is then worth relaxing this constraint and proceeding with an optimisation of both parameters $(\omega_2, \tau_e)$ at the same time with a fully numerical procedure, in order to verify the result and possibly extend them. To this end, we use the simplex search method implemented in the `fminsearch` function of Matlab, in order to find the values $(\omega_2^*, \tau_e^*)$ of $(\omega_2, \tau_e)$ that minimises the modulus of $H_1(\Omega)$ (defined by Eq. (11)) for all frequencies, with $\xi_1 = \xi_2 = 0$.

The result is illustrated in Fig. 11 for a particular value of $\mu$. One observes that for low values of $\kappa$, the two optimisation (the fixed-point one, $(\omega_2^{opt}, \tau_e^{opt2})$, shown in red, and the numerical one $(\omega_2^*, \tau_e^*)$, shown in orange) lead roughly to the same optimal frequency responses. On the contrary, for high values of $\kappa$, larger than $\kappa_{opt0}$, the numerical optimisation is able to realise a DVA+R-shunt absorber that slightly outperforms the standard mechanical DVA for any value of $\kappa$, since the orange surface is below the blue one, whereas the fixed-point optimisation was able to outperform the standard DVA only in a small range of coupling factors $\kappa \in [\kappa_{opt1}, \kappa_{opt2}]$. An example of this behaviour is shown in Fig. 13 for $(\mu, \kappa) = (0.05, 0.8)$, for which $\kappa > \kappa_{opt2}$. One observes that the numerically optimised DVA+R-shunt case (in dashed purple, $(\omega_2 = \omega_2^*, \tau_e = \tau_e^*)$) is slightly below the DVA case (green curve), also below the DVA+R-shunt with the fixed-point optimisation ($(\omega_2 = \omega_2^{opt}, \tau_e = \tau_e^{opt2})$, orange curve), which fails in this case. The red and blue curves are associated to the cases with the transducer in the open- and short-circuit, with $\omega_2 = \omega_2^*$. It can be observed that the fixed points $P_1$ and $P_3$ in this case no longer have the same amplitude, which is logical since $\omega_2^* \neq \omega_2^{opt}$. This illustrates that the equal fixed-point condition is not optimal in this case.

Figure 14 shows the evolution of the optimal parameters $(\omega_2, \tau_e)$, as a function of $\kappa$, for a given mass ratio ($\mu = 0.05$) and obtained with different criteria. The blue curves show the evolution of $\omega_2$, whereas the red curves show the evolution of $\tau_e$. The solid curves represent the numerically optimised parameters $(\omega_2^*, \tau_e^*)$, whereas the dotted curves

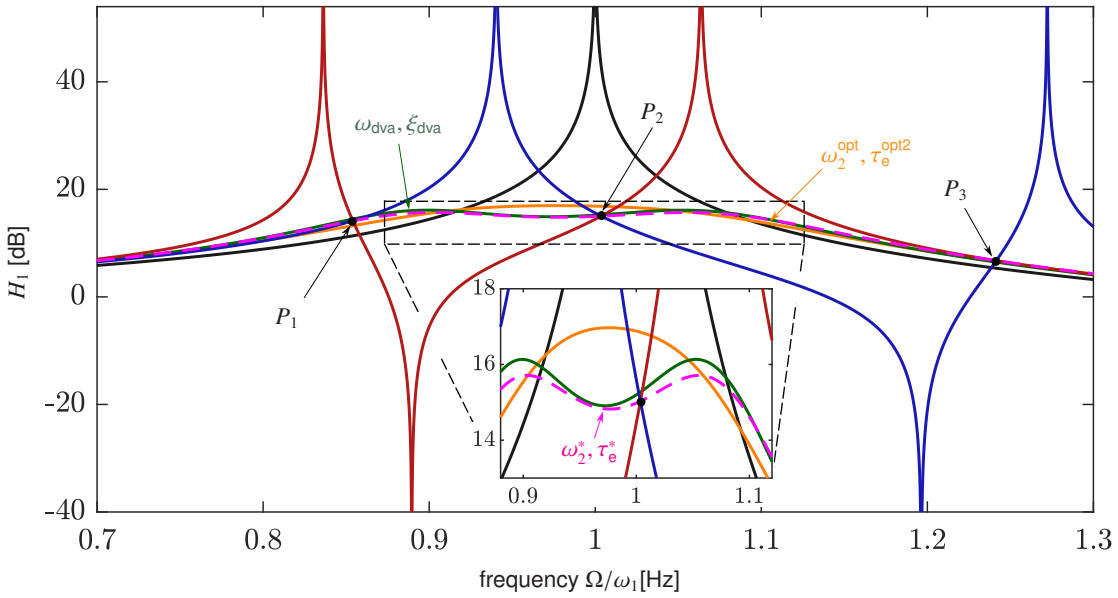



**Fig. 13:** Modulus of $H_1(\Omega)$ for $\xi_1 = \xi_2 = 0$ with $\mu = 0.05$ and $\kappa = 0.8$ under several conditions. (black curve): uncoupled primary structure (without DVA and EM-shunt); (orange curve): $\omega_2 = \omega_2^{opt} = 0.7951/\omega_1$ and $\tau_e = \tau_e^{opt2} = 0.83720/\omega_1$. (green curve) optimised DVA without EM shunt (its parameters follow Eqs. (21) and (28)). The other curves are obtained with $\omega_2 = \omega_2^* = 0.8895/\omega_1$ under different conditions: (red curve) transducer in open circuit ($\tau_e = 0$); (blue curve) transducer in short circuit ($\tau_e = +\infty$); (light purple dashed curve) $\tau_e = \tau_e^* = 0.4791/\omega_1$.

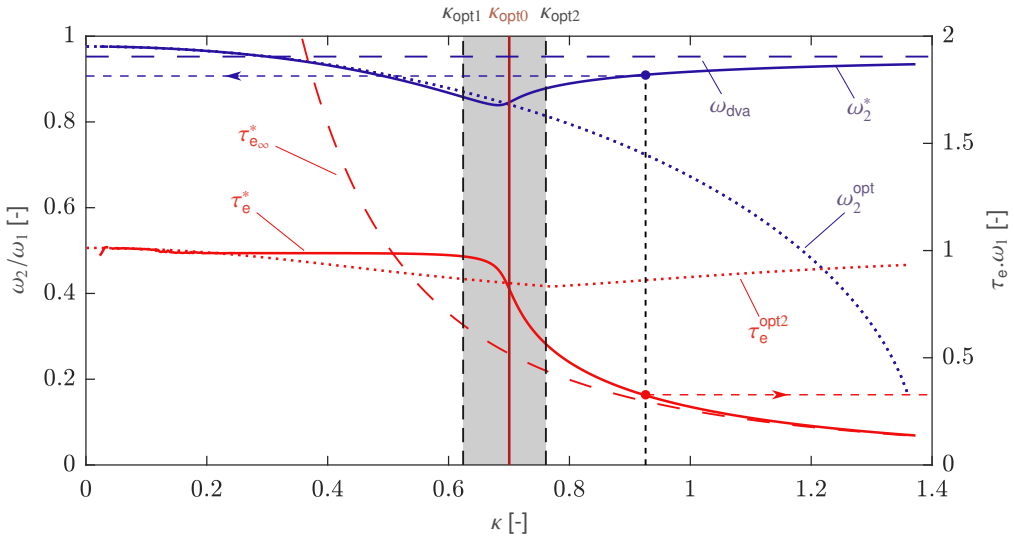



**Fig. 14:** Evolution of the optimal parameters ($\omega_2$ and $\tau_e$) as a function of $\kappa$ for $\mu = 0.05$. The blue curves show the evolution of $\omega_2$, whereas the red curves show the evolution of $\tau_e$. The solid curves represent $(\omega_2^*, \tau_e^*)$ obtained from numerical optimisation; dotted curves correspond to the parameters obtained using the fixed-point method $(\omega_2^{opt}, \tau_e^{opt2})$. The dashed curves indicate the asymptotic values $(\omega_{dva}, \tau_{e_\infty})$.

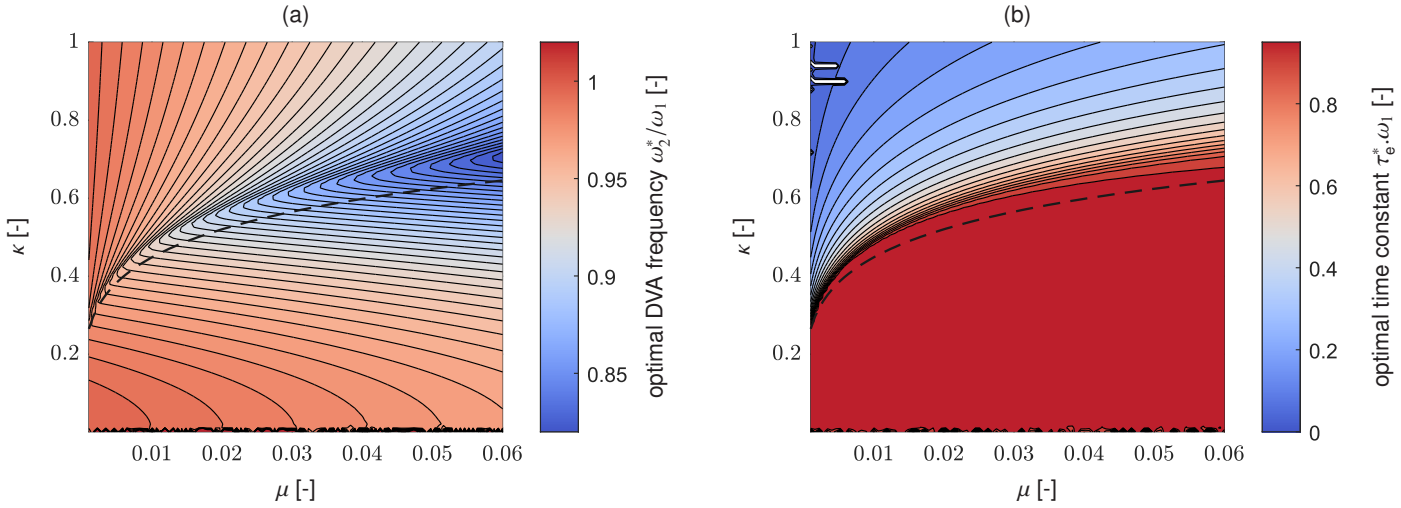



**Fig. 15:** Evolution of $\omega_2^*$ (a) and $\tau_e^*$ (b), scaled by $\omega_1$, as functions of $\mu$ and $\kappa$. The black dashed line indicates the optimal value $\kappa_{opt1}$ as a function of $\mu$: above this line, the DVA+R-shunt absorber outperforms a standard mechanical DVA.

show $(\omega_2^{opt}, \tau_e^{opt2})$ obtained using the fixed-point method presented previously. Finally, the dashed curves show the evolution of the parameters in the limit case where the inductive part of the transducer is neglected, for which the R-shunt is analogous to a purely mechanical dashpot (see Eq. (12)). The optimal parameters in this case satisfy:

$$\omega_2 = \omega_{dva}, \quad \tau_e = \tau_{e_\infty} = \frac{2\xi_{dva}\omega_{dva}}{\kappa^2\omega_1^2}. \tag{30}$$

It is observed that, for values of $\kappa$ lower than the gray zone ($\kappa < \kappa_{opt1}$), $\omega_2^*$ almost overlaps with the value of $\omega_2^{opt}$. For values above the gray zone, the two curves diverge from each other, for $\kappa > \kappa_{opt0}$. On the one hand, $\omega_2^{opt}$ decreases and tends to 0 for $\kappa = \sqrt{2/(1+\mu)} \simeq 1.38$ in this case (see Eq. (23)), whereas $\omega_2^*$ increases and tends towards $\omega_{dva}$. Regarding the evolution of $\tau_e^*$, similarly to $\omega_2$, for small values of $\kappa$, the curve of $\tau_e^*$ overlaps with that of $\tau_e^{opt2}$. The two curves begin to diverge for $\kappa > 0.2$, before crossing again around $\kappa_{opt0}$. The curve of $\tau_e^{opt2}$ tends towards 1 for large values of $\kappa$, whereas $\tau_e^*$ tends towards the curve of $\tau_{e_\infty}$.

Those results complement those of Fig. 11: for values of $\kappa$ below the gray zone, the fixed-point method leads to the optimal performances of the DVA+R-shunt, but they remain lower than that of an optimised mechanical DVA. However, for values of $\kappa$ above the gray zone, it is possible to obtain a DVA+R-shunt with equivalent (though slightly better) performance than a mechanical DVA, at the condition of detuning the R-shunt frequency $\omega_2$ with respect to $\omega_2^{opt}$ obtained by the fixed point method. One can observe in Fig. 11 that the amplitude of the orange surface at the external fixed point frequencies are no more equal, whereas this surface is below the blue one. As a final remark, one can observe that the high values of the EMCF case ($\kappa$ larger than the gray zone) behaves as if the inductive behaviour of the transducer were neglected, for which the R-shunt is equivalent to a pure viscous damper, since $\omega_2^* \to \omega_{dva}$ and $\tau_e^* \to \tau_{e\infty}^*$, as already addressed in [24].

### 3.2.5 Summary for the displacement $H_\infty$ optimisation

As seen in previous sections, for each value of $\mu$, there is a range of values of the EMCF $\kappa \in [\kappa_{opt1}, \kappa_{opt2}]$ for which the fixed point optimisation $(\omega_2 = \omega_2^{opt}, \tau_e = \tau_e^{opt2})$ guarantees a DVA+R-shunt absorber with better performance than an optimised mechanical DVA. Then, above this range, it is still possible to have a DVA+R-shunt with better performances by relaxing the fixed point condition and numerically optimising the parameters such that $(\omega_2 = \omega_2^*, \tau_e = \tau_e^*)$. Consequently, for each value of $\kappa$ and $\mu$, it is possible to find optimal values of the DVA's natural frequency $\omega_2$ and the electrical time constant $\tau_e$. Those results are gathered in Fig. 15, obtained by numerical optimisation. It can be considered as a tuning chart for the DVA+R-shunt absorber. Notice that in the area below the black dashed curve, for which $\kappa < \kappa_{opt1}$, the fixed point optimisation is valid and the plots are almost identical to those of Figs. 3 and 8(a) (with different color ranges).

Finally, it is of interest to consider the limit case for which $\kappa = \kappa_{opt1}$. In this case, for a given value of $\mu$, one can find with the fixed point method a set of optimal values $(\omega_2^{opt}, \kappa_{opt1}, \tau_e^{opt2})$ of the parameters to obtain a DVA+R-shunt as

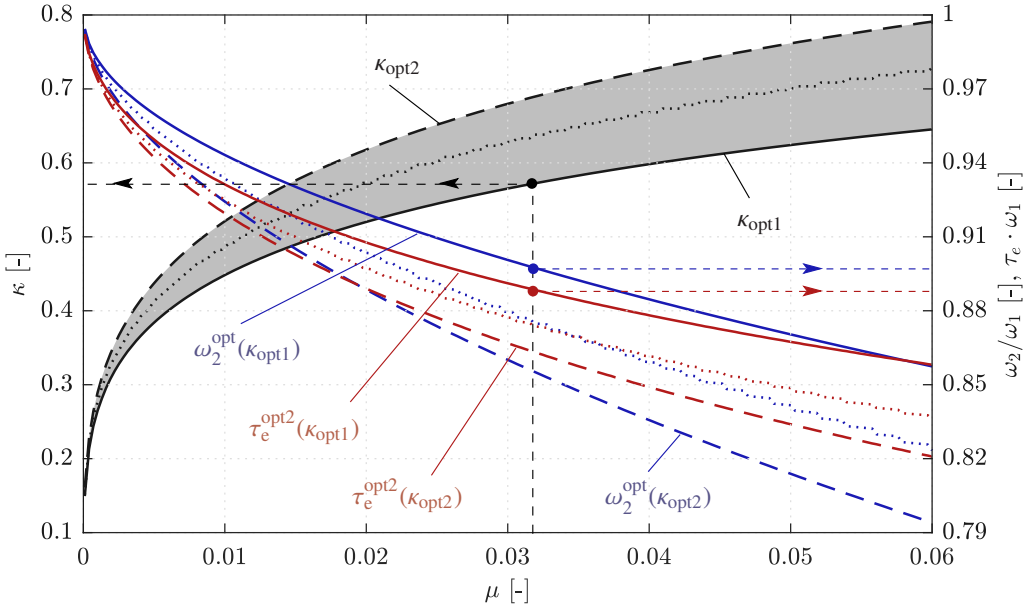



**Fig. 16:** Tuning graph of a DVA+R-shunt absorber: optimal values $\kappa_{opt}$ of the EMCF (black curves and left y-axis), that has to be chosen in the gray area, as a function of the mass ratio $\mu$. Corresponding values of the DVA's natural frequency $\omega_2^{opt}$ (blue curves) and the electrical time constant $\tau_e^{opt2}$ (red curves), both scaled by $\omega_1$ and readable in the right y-axis. The value $\kappa_{opt0}$ that leads to the best DVA+R-shunt performance is also indicated by the dotted curves.

performant as an optimal mechanical DVA and with a minimal EMCF. Its value can be read as a function of $\mu$ thanks to the black solid line and the left axis in Fig. 16, whereas the corresponding values of the two other parameters $\omega_2^{opt}(\kappa_{opt1})$, $\tau_e^{opt2}(\kappa_{opt1})$ are read on the right axis. Then, for a particular transducer and a primary system such that $\kappa > \kappa_{opt1}$, it is still possible to to obtain a DVA+R-shunt as performant as an optimal mechanical DVA by numerically optimising it and choosing $(\omega_2 = \omega_2^*, \tau_e = \tau_e^*)$. Figure 16 can be thus considered as a tuning graph useful for practical applications.

## 3.3 Performance with non-zero damping in the primary structure

Real structures have a non-zero damping coefficient ($\xi_1 \neq 0$). This makes it possible to define a performance indicator called the *attenuation* and already used in previous studies [43, 19, 44, 23]:

$$A_{dB} = 20 \log_{10} \left| \frac{H_{naked}}{H_{abs}} \right|, \tag{31}$$

where $H_{naked}$ is the peak amplitude of $|H_1(\Omega)|$ with the primary structure naked (without absorber) and with damping ($\xi_1 \neq 0$), $H_{naked} \simeq 1/(2\xi_1)$ and $H_{abs}$ is its maximum with an absorber connected and optimally tuned. Consequently, $A_{dB}$ is the difference between the primary structure's responses without and with the absorber, as illustrated in Fig. 17(a). Then, Fig. 17(b) presents the attenuation $A_{dB}$ for both the optimised DVA and the proposed absorber (the DVA+R-shunt optimally tuned with $(\kappa, \omega_2, \tau_e) = (\kappa_{opt0}, \omega_2^{opt}, \tau_e^{opt2})$) as a function of $\xi_1$ for a given value of $\mu$. This plot shows that the proposed absorber performs equivalently than an optimised DVA, with even a slight outperformance.

Figure 17(a) shows a remarkable result: the optimisation proposed in Sections 3.1 and 3.2, established by neglecting the primary structure's damping $\xi_1$, is still valid even in the case of a non-zero primary structure damping. This result is then confirmed for different pairs of $(\mu, \xi_1)$ in Fig. 17(b).

## 3.4 Performance with non-zero damping in the DVA

The DVA+R-shunt optimisation proposed in the previous sections was conducted by neglecting the damping ratio of the DVA ($\xi_2 = 0$). In practical applications, $\xi_2$ is always non-zero. However, if no additional mechanical damping device (oil damper, viscoelastic material…) is included, $\xi_2$ can be considered small, such that the optimisation of the previous sections may still be valid. To evaluate this point, the difference between the attenuation $A_{abs}$ brought by a

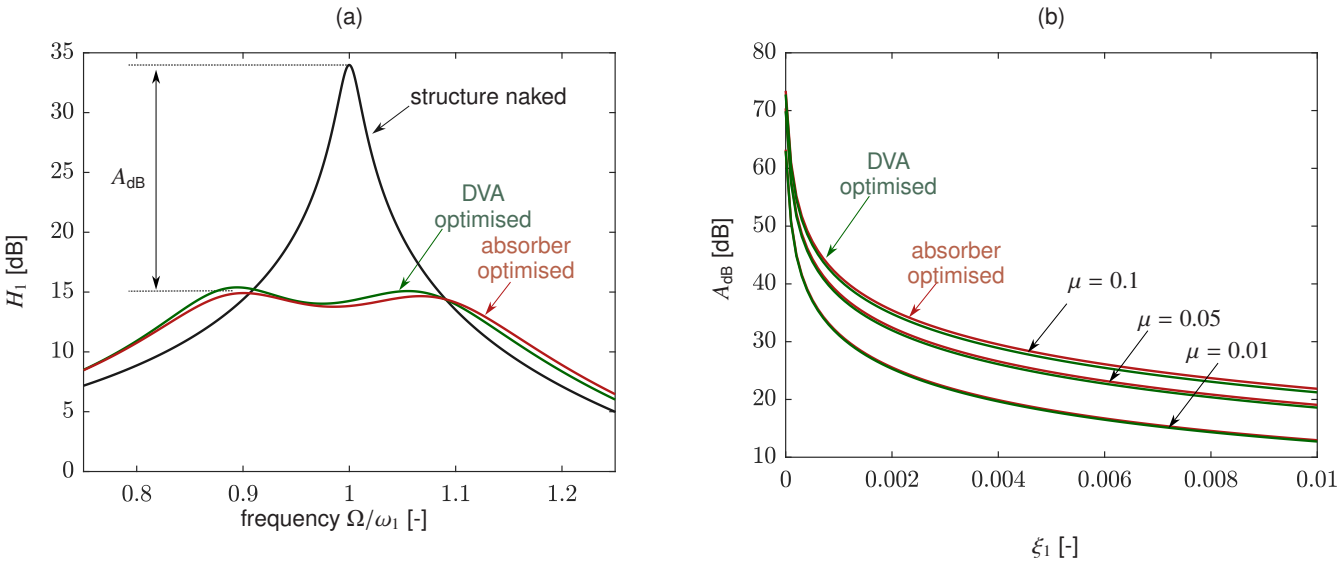



**Fig. 17:** (a) Modulus of the frequency response function $H_1(\Omega)$ with a non-zero damping coefficient of the primary structure $\xi_1 = 1\%$, shown under different conditions: (black curve) uncoupled primary structure; (green curve) optimised mechanical DVA ($(\omega_2, \xi_2) = (\omega_{\text{dva}}, \xi_{\text{dva}})$); (orange curve) optimised DVA+R-shunt ($(\omega_2, \kappa, \tau_{\text{e}}) = (\omega_2^{\text{opt}}, \kappa_{\text{opt}}, \tau_{\text{e}}^{\text{opt2}})$ and $\xi_2 = 0$). (b) Variation of $A_{\text{dB}}$ as a function of the damping coefficient $\xi_1$ of the primary structure and the mass ratio $\mu$ for an optimised mechanical DVA (green curves) and the optimised DVA+R-shunt absorber (orange curves).

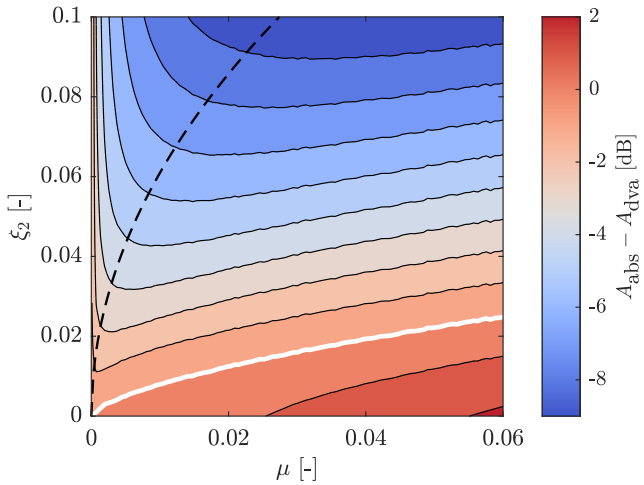



**Fig. 18:** Evolution of $\delta$ (see Eq. (32)) as a function of $\mu$ and $\xi_2$ for a primary structure whose damping coefficient is $\xi_1 = 0.25\%$. The white curve highlights $\xi_2(\mu)$ for which $\delta = 0$. The black dashed curve indicates $\xi_{\text{dva}}(\mu)$ (Eq. (28)).

DVA+R-shunt optimally tuned (with $(\kappa, \omega_2, \tau_e) = (\kappa_{opt0}, \omega_2^{opt}, \tau_e^{opt2})$ but with a non zero $\xi_2$) and the one brought by an optimal mechanical DVA (with $(\omega_2, \xi_2) = (\omega_{dva}, \xi_{dva})$) is defined as:

$$\delta = A_{abs} - A_{dva}. \tag{32}$$

Then, Fig. 18 shows $\delta$ as a function of $\mu$ and $\xi_2$ (notice that $A_{dva}$ does not depend on $\xi_2$ since $\xi_2 = \xi_{dva}$ for $A_{dva}$). One can first observe that a threshold value of $\xi_2$ exists, shown by the white curve, below which the DVA+R-shunt absorber performs better ($\delta > 0$) than the mechanical DVA. This is logical since the EMCF was chosen such that $\kappa = \kappa_{opt0}$ to compute $A_{abs}$. Above this threshold, the DVA+R-shunt's performances decrease as a function of $\xi_2$, but the difference in dB remains small with respect to the mechanical DVA for low values of $\xi_2$. In particular, the internal damping of a mechanical DVA with elastic components often leads to a damping ratio smaller than $1\%$ ($\xi_2 < 0.01$). In this case, Fig. 18 shows that the loss of performance of the DVA+R-shunt absorber is less than 1 dB. As a consequence, the optimisation proposed in Sections 3.1 and 3.2, obtained with $\xi_2 = 0$, can still be considered valid if R-shunt is used to optimally tune the damping of a mechanical DVA without additional mechanical damping device. Figure 18 also shows in dashed black the optimal value $\xi_{dva}$ of $\xi_2$ for an optimal mechanical DVA, which are much higher than $1\%$ for standard values of $\mu < 0.5\%$.

If the DVA+R-shunt absorber is used to correct a mechanical DVA that has a large intrinsic damping $\xi_2$, or to act in parallel to a mechanical damping device already installed in the DVA, a numerical optimisation of its parameters $(\kappa, \omega_2, \tau_e)$ with $\xi_2 \neq 0$ may be useful. This question is left for a subsequent study.

# 4 Absorber optimisation to reduce the acceleration of the primary structure

The goal of this section is to reconsider the optimisation of the absorber presented in the previous section under a new criterion: instead of considering an $H_\infty$-optimisation on the displacement of the primary structure, we consider here reducing its maximal *acceleration*. This has been considered in a previous work about resonant piezoelectric shunts [20] and acceleration is an interesting criteria for vibration reduction since it is the most perceptible by humans [45, 46]. It is also useful since the measurements of Section 5 are made in acceleration.

We still consider the system of Fig. 1. Since the displacement and acceleration responses of a structure are related with a $\Omega^2$ relationship ($\hat{\gamma}_1(\Omega) = -\Omega^2 \hat{x}_1(\Omega)$ where $\gamma_1(t) = \ddot{x}_1(t)$ denotes the acceleration of the primary structure), the shape of the corresponding frequency response is not the same. Precisely, the dimensionless accelerance of the primary structure is defined as:

$$\tilde{H}_1(\Omega) = \frac{\hat{\gamma}_1(\Omega)}{\hat{\gamma}_1(\Omega \to +\infty)} = -\frac{\Omega^2}{\omega_1^2} H_1(\Omega). \tag{33}$$

where the $\Omega^2$ difference clearly appears. This difference leads to different optimal parameters of the DVA+R-shunt absorber than those obtained in the previous section, in order to reduce the maximum of $|\tilde{H}_1(\Omega)|$ as much as possible.

It is important to note that the $\Omega^2$ dependence of $\tilde{H}_1$ with respect to $H_1$ does not affect Eq. (15), such that $|\tilde{H}_1(\Omega)|$ also shows three fixed points at the same frequencies $\Omega_{P_1}$, $\Omega_{P_2}$ and $\Omega_{P_3}$, with differences the corresponding amplitude of $|\tilde{H}_1(\Omega)|$. Consequently, the same methodology than in Section 3 is now applied to $|\tilde{H}_1(\Omega)|$.

## 4.1 Optimisation of $\omega_2$

As in Section 3.1, the optimal value $\tilde{\omega}_2^{opt}$ for the present accelerance optimisation is defined as the value of $\omega_2$ that allows the external fixed points ($P_1$ and $P_3$) to be at the same amplitude in the mechanical conservative context ($\xi_1 = \xi_2 = 0$). This leads to:

$$|\tilde{H}_1(\Omega_{P_1})| = |\tilde{H}_1(\Omega_{P_3})| \Leftrightarrow \Omega_{P_1}^2 |H_1(\Omega_{P_1})| = \Omega_{P_3}^2 |H_1(\Omega_{P_3})|, \tag{34}$$

which leads to an optimal value $\tilde{\omega}_2^{opt}$ in the present accelerance case different than $\omega_2^{opt}$ obtained with the displacement criterion (compare Eq. (34) with (20)).

Computing $\tilde{\omega}_2^{opt}$ numerically with the same strategy than in Section 3.1 and observing the result in the accelerance of the primary mass leads to Fig. 19(b). One observes that if $\omega_2 = \tilde{\omega}_2^{opt}$, changing the values of the other parameters does not change the frequency of the central fixed point, that remains equal to the natural frequency of the primary system:

$$\Omega_{P_2} = \omega_1. \tag{35}$$

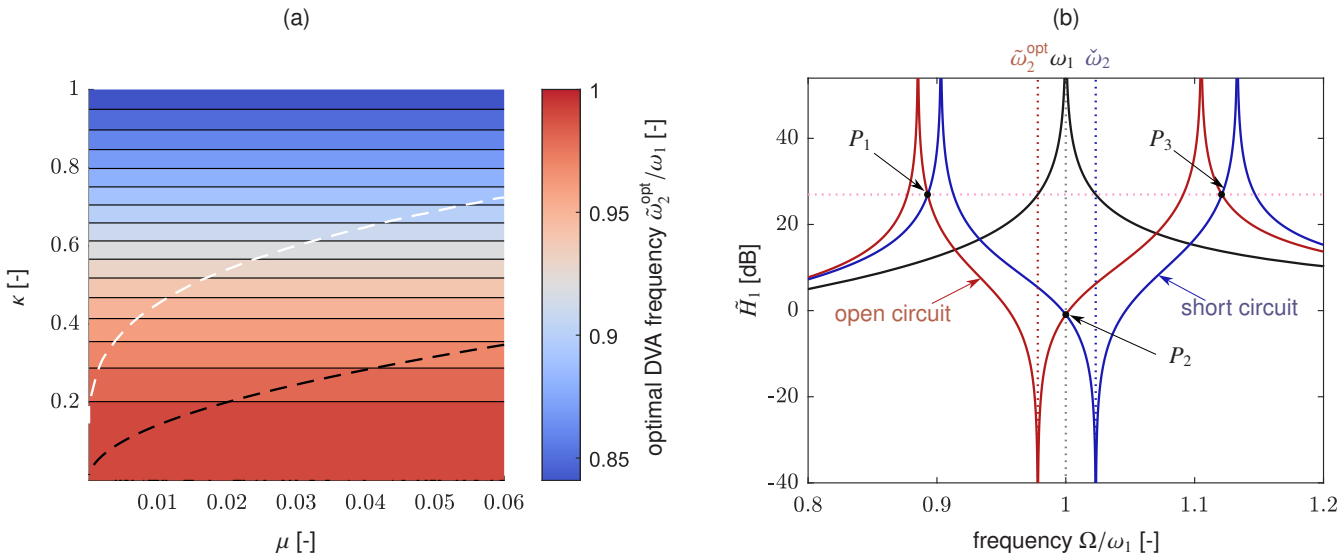



**Fig. 19:** Optimisation of $\omega_2$ for the accelerance criterion. (a) Evolution of $\tilde{\omega}_2^{opt}/\omega_1$ as a function of $\mu$ and $\kappa$. The black dashed curve shows the threshold value below which $\tilde{\omega}_2^{opt}$ exceeds the classical optimal value for a DVA $\tilde{\omega}_{dva}$ (see Eq. (37)). The white dashed curve marks the threshold above which the amplitude of the central fixed point $P_2$ is higher than that of $P_1$ and $P_3$. (b) Modulus of $\tilde{H}_1$ of the system in Fig. 1 with $\xi_1 = \xi_2 = 0$ and $\omega_2 = \tilde{\omega}_2^{opt}$ under several conditions. (black dashed curve): uncoupled primary structure (without DVA and EM-shunt); (red curve): transducer in open circuit ($\tau_e = 0$); (blue curve): transducer in short circuit ($\tau_e = +\infty$). The parameter are $\mu = 0.05$ and $\kappa = 0.3$.

A similar result has been obtained in Section 3.1, for which $\Omega_{P_2}$ was equal to $\omega_{1,\infty}$. With an analogous procedure than the one used to obtain Eq. (23) for $\omega_2^{opt}$, one obtains the following closed form expression:

$$\tilde{\omega}_2^{opt} = \omega_1 \sqrt{\frac{1-\kappa^2}{2} + \frac{\sqrt{\kappa^4+1}}{2}}. \tag{36}$$

This result was confirmed by numerical simulations. Similarly to the displacement case, this expression can be derived analytically, and the corresponding method is presented in Appendix B. It is illustrated in Fig. 19(a) which shows $\tilde{\omega}_2^{opt}$ scaled by $\omega_1$ as a function of the two independent parameters $(\mu, \kappa)$. As in Fig. 3 for the displacement criterion, $\tilde{\omega}_2^{opt}$ takes a different value, that depends on $\kappa$, than the optimal one for a mechanical DVA optimised in accelerance, that reads [47]:

$$\tilde{\omega}_{dva} = \frac{\omega_1}{\sqrt{1+\mu}}. \tag{37}$$

The black dashed curve in Fig. 19(a) indicates the threshold above which $\tilde{\omega}_2^{opt}$ is larger than $\tilde{\omega}_{dva}$.

A noticeable observation is that $\tilde{\omega}_2^{opt}$ is independent of $\mu$. Moreover, one can also observe that the optimal natural frequency in the present accelerance case is larger than in the displacement case for a given value of $(\kappa, \mu)$: $\tilde{\omega}_2^{opt}(\kappa,\mu) > \omega_2^{opt}(\kappa,\mu)$. It is also the case for a mechanical DVA: $\tilde{\omega}_{dva}(\mu) > \omega_{dva}(\mu)$.

## 4.2 Optimisation of $\tau_e$ and $\kappa$

As in Section 3.2, we proceed by optimising successively $\tau_e$ and then $\kappa$. For $\tau_e$ optimisation, the second strategy, fully numerical and presented in of Section 3.2.2, is selected here since it gives better results. The obtained values of $\tau_e$, denoted as $\tilde{\tau}_e^{opt2}$, are given in Fig. 20(a) as a contour plot in the $(\mu, \kappa)$ plane.

A representative case is shown in Fig. 20(b), where the acceleration response of the primary system is represented under several conditions. One can observe that the case with $(\omega_2, \tau_e) = (\tilde{\omega}_2^{opt}, \tilde{\tau}_e^{opt2})$ is optimal since the orange curve has its two maxima close to the fixed points, but performs lesser than an optimised mechanical DVA since the EMCF $\kappa$ is not optimal. The optimal parameters for the DVA in the present accelerance case are $\omega_2 = \omega_{dva}$ of Eq. (37) and $\xi_2$ defined as [47]:

$$\tilde{\xi}_{dva} = \sqrt{\frac{3\mu}{4(2+\mu)}}. \tag{38}$$

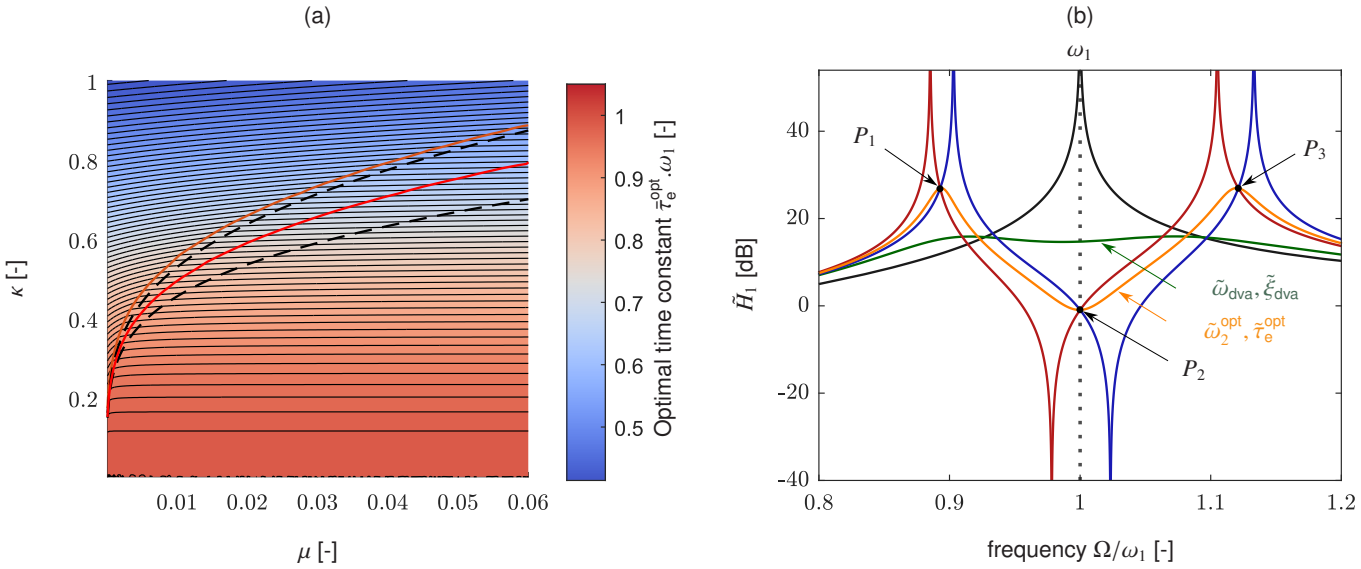



**Fig. 20:** (a) Evolution of the time constant optimal value $\tilde{\tau}_e^{opt}$, scaled by $\omega_1$, as a function of $(\mu, \kappa)$. The red curve shows the optimised value $\tilde{\kappa}_{opt}$ of $\kappa$ as a function of $\mu$. The area between the two dashed black curve corresponds to values of $(\mu, \kappa)$ for which the DVA+R-shunt absorber has better performance than a standard mechanical DVA. The orange curve limits the number of extrema of $|\tilde{H}_1|$: above, it has one maximum and below it has two maxima and one minimum. (b) Modulus of $\tilde{H}_1(\Omega)$ with $\xi_1 = \xi_2 = 0$ and $\omega_2 = \tilde{\omega}_2^{opt}$ under several conditions. (black dashed curve): uncoupled primary structure (without DVA and EM-shunt); (red line): transducer in open circuit ($\tau_e = 0$); (blue line): transducer in short circuit ($\tau_e \to +\infty$); (orange line): $\tau_e = \tilde{\tau}_e^{opt} = 0.9343/\omega_1$; (green dashed line) optimised DVA without EM shunt (its parameters follow Eqs. (37) and (38)). The parameters are $\mu = 0.05$ and $\kappa = 0.3$.

Consequently, as in Section 3.2.2, it is possible to determine an optimal value of $\kappa$, named $\tilde{\kappa}_{opt}(\mu)$, for which the reduction of vibrations is maximised. This curve is plotted in red in Fig. 20(a). In addition, for each value of $\mu$, there is an interval $[\tilde{\kappa}_{opt_1}, \tilde{\kappa}_{opt_2}]$ in which the DVA+R-shunt absorber is more efficient than a single mechanical DVA. It corresponds to the area in Fig. 20(a) between the two dashed black curves. Furthermore, the orange curve shows the value of $\kappa$ for which the number of stationary points of $|\tilde{H}_1|$ changes (see Fig. 12(a)).

It is also possible to compute the amplitude of $\tilde{H}_1$ at the fixed point $P_2$:

$$|\tilde{H}_1(\Omega_{P_2})| = \frac{\sqrt{\kappa^4 + 1} - 1}{\kappa^2 \mu}, \tag{39}$$

obtained using Eqs. (35) and (36) in (33) and (14) with $\tau_e = 0$.

### 4.3 System's behaviour with non-zero damping in the primary structure

As in Section 3.3, it is possible to measure the effectiveness of the DVA+R-shunt absorber in the case of a damped primary structure and to compare it to the one of a mechanical DVA. To this end, an attenuation parameter $\tilde{A}_{dB}$ is defined by the following equation, similar to $A_{dB}$ of Eq. (31):

$$\tilde{A}_{dB} = 20 \log_{10} \left| \frac{\tilde{H}_{naked}}{\tilde{H}_{abs}} \right|, \tag{40}$$

where $\tilde{H}_{naked}$ and $\tilde{H}_{abs}$ are defined as $H_{naked}$ and $H_{abs}$ by replacing $H_1(\Omega)$ by $\tilde{H}_1(\Omega)$. It is then possible to plot $\tilde{A}_{dB}$ as a function of $(\xi_1, \mu)$ and to compare the result for both absorbers (the present DVA+R-shunt one and an optimise DVA). A plot identical to Fig. 17(b) is obtained (it is not reproduced here for the sake of conciseness), leading also to similar conclusions.

## 5 Experimental validation

This section presents the experimental implementation of the absorber device (DVA + R-shunt) on a mechanical structure. After introducing the experimental apparatus, the observation of the damping compensation of a DVA thanks

| Modal parameters of the structure (mode 1) | | |
|---|---|---|
| Modal mass | $m_1$ | 3.82 kg |
| Natural frequency | $\omega_1/(2\pi)$ | 26.69 Hz |
| Modal damping ratio | $\xi_1$ | 0.25% |
| Parameters of the DVA | | |
| Mass of the support | $m_{\text{base}}$ | 0.156 kg |
| Mass at the end of the beam | $m_{\text{dva}} \simeq m_2$ | 0.204 kg |
| Mass ratio | $\mu = m_2/m_1$ | 0.0534 |
| Damping ratio | $\xi_2$ | 0.45% |
| Electromechanical parameters of the EM transducer | | |
| Inductance | $L_t$ | 657 µH |
| Resistance | $R_t$ | 3.2 Ω |
| Force factor | $\phi_t$ | 2.2 N/A |
| EM coupling factor (Eq. (5)) | $\kappa$ | 1.133 |

**Table 1:** Electromechanical parameters of the experimental apparatus of Fig. 21.

to an R-shunt is described. Then, the optimisation of the device absorber parameters ($\omega_2$, $\tau_e$, and $\kappa$) is performed to minimise the maximum value of the frequency response function of the mechanical structure's acceleration.

## 5.1 Experimental setup

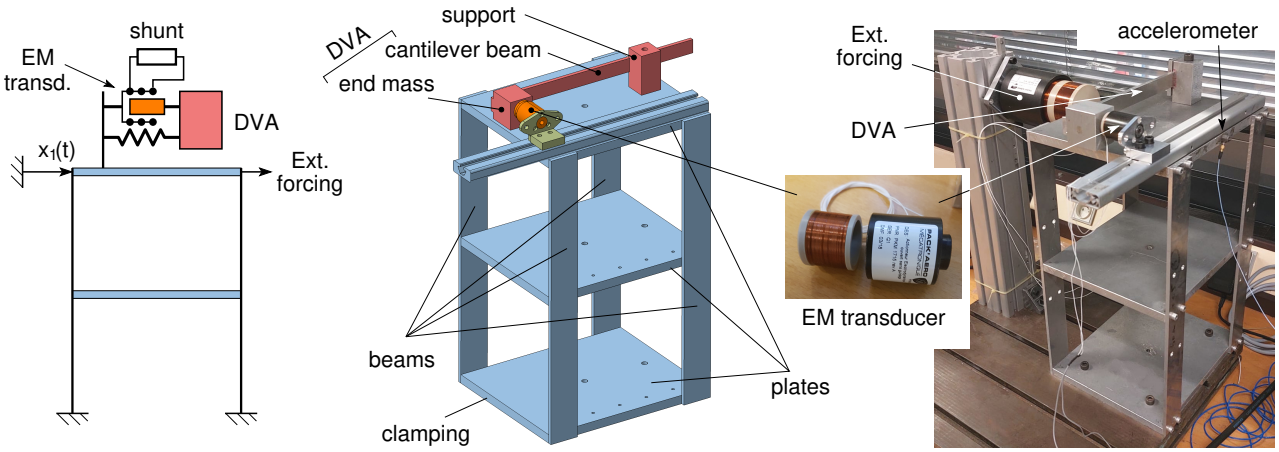



**Fig. 21:** Diagram and picture of the experimental setup

The experimental setup is shown in Fig. 21. The mechanical structure is the same as the one already used in [23, 6]. It consists of three identical plates, acting as inertias, linked to each other by four identical elastic beams, acting as springs. Thanks to an experimental modal analysis, the two first modes are identified as bending modes, for which the two upper plates move either in phase or in phase opposition (see the mode shapes in [23, 6]). All the tests of this section will be performed around the resonance of the first (in-phase) bending mode, which identified characteristics are given in Tab. 1. Those parameters were identified by measuring the collocated FRF of the top plate (with DVA support, rail and permanent magnet attached and without the DVA's beam and end mass) with a hammer test, and fitting the one degree of freedom model of Eq. (4a) (with $\mu = 0$) to the result.

A DVA is installed at the top of the structure. It consists of an aluminium cantilever beam with a mass $m_{\text{dva}} \simeq m_2$ attached to one of its ends and bolted to the upper plate at the other end, thanks to a parallelepiped shaped support. The mass of this support is included in the modal mass $m_1$ of the structure's first mode. The natural frequency $\omega_2$ of the DVA can be adjusted by modifying the length between the end mass and the bolted joint. Furthermore, an EM transducer (a PACKAERO PKM 1715 voice coil) is placed between the upper plate and the end mass of the DVA, at an adjustable position thanks to several bolted elements and a rail. The permanent magnet and the coil are respectively attached to the upper plate and the DVA's end mass. Consequently, the coil is free to move in a magnetic radial field created by the permanent magnet. The parameters of the transducer are reported in Tab. 1. The inductance $L_t$ and

resistance $R_t$ were obtained by measuring the electrical admittance at the coil's terminals and fitting the model of Eq. (1), $R_t$ being associated to the internal resistance of the coil and the wires. Then, the force factor $\phi_t$ was fitted with the open-circuit FRF of the system (see the red curve of Fig. 22 that will be analysed in the next section).

To provide a mechanical external forcing, another voice coil (PACKAERO PKM 2001) is used, with its coil fixed to the upper plate and its permanent magnet attached to a vertical column linked to the frame. In all subsequent analyses, a periodic chirp signal will be used to drive the structure in vibrations, through a Brüel & Kjær 4806 power amplifier. The electric current $I_{exc}(t)$ that is fed to the exciter's coil by the power amplifier is measured by a current clamp. Since it is proportional to the force acting on the structure, this signal will be used as a reference for the frequency response functions (FRFs). An accelerometer (PCB Piezotronics 352C65) is fixed to the upper plate to measure its acceleration $\gamma_1(t) = \ddot{x}_1(t)$. Thanks to those two signals, the FRF $\hat{\gamma}_1/\hat{I}_{exc}$ of the primary system is estimated in a standard way thanks to an $H_1$ estimate and several averaging [48].

As the following sections are dedicated to validate the optimisations proposed in Sections 3 and 4, the resistance and inductance of the R-shunt will have to be modified to adjust the parameters $\tau_e$ and $\kappa$. To this end, it has been chosen to use a real time controller instead of relying to analog electronics. A dSPACE CP1104 real time controller with the simulated circuit implemented as a Matlab Simulink diagram is used, along with a TŒLLNER TOE 7621 four quadrants amplifier for the power interface with the transducer.

## 5.2 Variation of electrical resistance with $\omega_2 = \tilde{\omega}_2^{\text{opt}}$

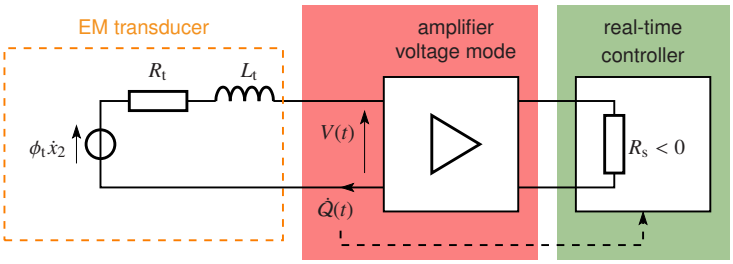



**Fig. 22:** Diagram of the electrical circuit of the transducer with the simulated resistance.

In this section, the focus is on the optimisation of $\omega_2$ and $\tau_e$ for the given values of $\mu = 0.0534$ and $\kappa = 1.133$ of the system (see Tab. 1). Since our measurements are accelerances, the aim is to validate the theoretical results of Section 4.

The first step is to adjust the DVA's natural frequency. Using Eq. (36), one obtains $\tilde{\omega}_2 = 0.8196\omega_1$ ($\omega_2/(2\pi) = 21.87$ Hz). This frequency is tuned by adjusting the length of the cantilever beam of the DVA. The second steps is to adjust the electrical time constant at the value $\tilde{\tau}_e^{\text{opt}} = 0.2933/\omega_1 = 1.749$ ms, calculated numerically as explained in Section 4.2. Notice that this value could be read in the upper part of the graph of Fig. 20(a), not shown since restricted to values of $\kappa$ lower to 1. Since $\tilde{\tau}_e^{\text{opt}} = L_t/R_{\text{opt}}$, one obtains an optimal equivalent resistance of the circuit $R_{\text{opt}} = 0.376\ \Omega$ according to the inductance of the transducer $L_t$ (see Tab. 1). This value is less that the transducer resistance $R_t$. In order to address this issue, the real time controller is used to simulate a negative compensating resistance $R_s < 0$, such that $R_{\text{opt}} = R_t + R_s$.

A diagram of the setup is presented in Fig. 22. The electrical current $\dot{Q}$ in the EM transducer is measured thanks to the current monitor of the amplifier. Then, thanks to the voltage mode of the amplifier, the voltage signal $V(t) = R_s\dot{Q}(t)$, with $R_s < 0$, is created by the real-time controller and prescribed at the terminals of the EM transducer.

Figure 23 shows the modulus of primary structure's FRF $|\hat{\gamma}_1/\hat{I}_{exc}|$ in several configurations. First of all, the black curve shows the frequency response of the structure without absorber. One first observes that the modal model, shown in black dashed curve, perfectly fits the experiments with the identified values of the parameters $(\omega_1, \xi_1)$ (see Tab. 1). Notice that the amplitude of the FRF was manually adjusted to the best fit since the force factor of the voice coil used for the excitation was not measured. The value of $m_1$ is thus not involved here.

The red curve shows the case with the DVA coupled to the transducer in open circuit condition. Again, the dashed red curve, presenting the theoretical results, globally fits well the experiments. Then, the gradient curves from red to blue show the FRF for different $R_s$ values, simulated with the real time controller. The more the colour tends towards blue, the greater the negative compensation resistance is. Those variation clearly make the three fixed points $P_1$, $P_2$ and $P_3$ appear. One can also observe that the two external fixed points ($P_1$ and $P_3$) are almost at the same

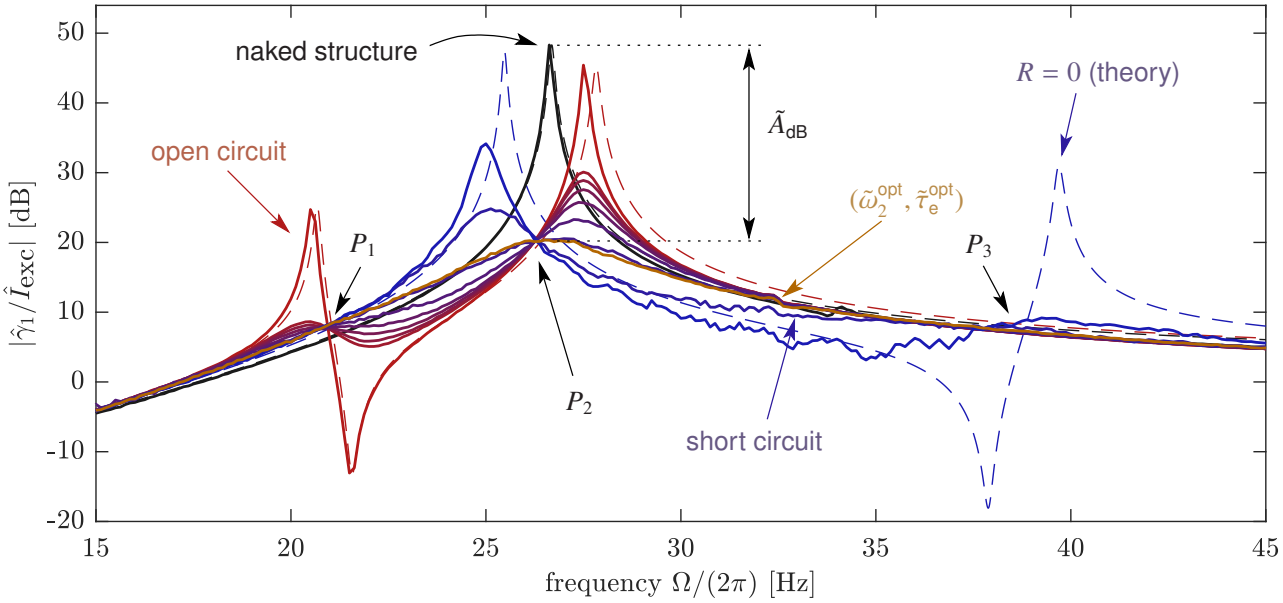



**Fig. 23:** Experimental modulus of FRF $\hat{\gamma}_1/\hat{I}_{\text{exc}}$ of the mechanical structure under several conditions, with the natural frequency of the DVA optimised ($\omega_2 = \tilde{\omega}_2^{\text{opt}}$) and with the real time controller that simulates a negative resistance (Fig. 22). (black line): uncoupled primary structure (without DVA and EM-shunt) and (black dashed line) associated theoretical curve; (red line): transducer in open circuit; (gradient curves from red to blue): different value of $R_{\text{s}}$; (red dashed line): theoretical open circuit case; (blue dashed line): theoretical $R = 0$ case; (gold curve) optimal electrical time constant ($\tau_{\text{e}} = \tilde{\tau}_{\text{e}}^{\text{opt}}$).

amplitude, validating the DVA tuning (the optimised value $\tilde{\omega}_2$). The point $P_2$ appears close to the natural frequency of the structure naked, which is coherent with the theoretical observation of Section 4.1.

The case with the transducer short-circuited, meaning that $R = R_{\text{t}}$, is also shown by a blue curve in Fig. 23. Interestingly, because $R_{\text{t}}$ is not small, the $P_3$ fixed point is not noticeable in this case. It appears with the blue dashed curves, that shows the result with a zero theoretical resistance $R = 0$, associated to an infinite time constant $\tau_{\text{e}} \to +\infty$. In between those two curves, by increasing the negative simulated resistance $R_s$ as much as possible, and as close as possible to the instability achieved when $R = R_{\text{t}} + R_{\text{s}} \simeq 0$, it was possible to measure another FRF, which approaches the theoretical $R = 0$ case.

Finally, the gold curve shows the FRF with the optimal value $\tau_{\text{e}} = \tilde{\tau}_{\text{e}}^{\text{opt}}$. Because $\kappa$ is large in this case, larger that $\tilde{\kappa}_{\text{opt2}} \simeq 0.8$ (see Fig. 20(a)), the FRF has only one extrema at $\Omega = \Omega_{P_2}$, which clearly appears in the plot. For this optimal case, the attenuation $\tilde{A}_{\text{dB}}$ can be estimated with Eq. (39) that gives the amplitude of $\tilde{H}_1(\Omega_{P_2} = \omega_1)$, such that $A_{\text{dB}} = -20\log_{10}[2\xi_1\tilde{H}_1(\omega_1)] = 26.8$ dB (remember that the peak amplitude of the naked structure's FRF is $1/(2\xi_1)$), which is coherent with the experimental results.

## 5.3 Optimisation of $\kappa$ by simulated inductance

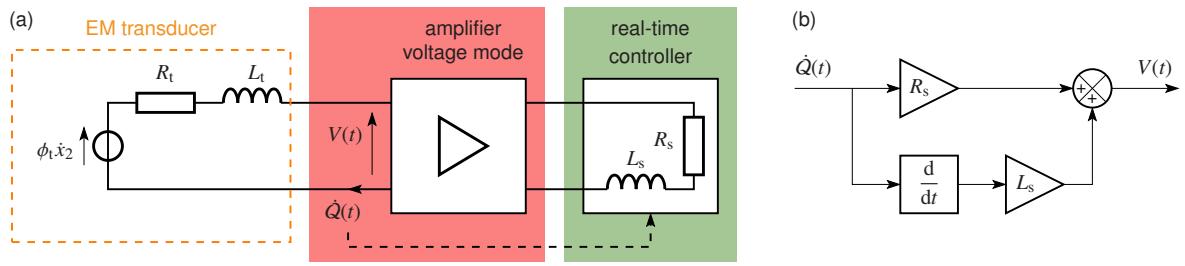



**Fig. 24:** (a) Diagram of the electrical circuit of the transducer with the simulated resistance and inductance. (b) Block diagram of the real-time controller.

As explained in Sections 3.2.3 and 4.2, there is a range of values of $\kappa \in [\tilde{\kappa}_{\text{opt1}}, \tilde{\kappa}_{\text{opt2}}]$ for which the performance of the DVA+R-shunt absorber are better than those of an optimised mechanical DVA. Figure 20(a) shows that for the

present value of the mass ratio $\mu = 0.0534$, $\kappa_{\text{opt2}} \simeq 0.8$ (corresponding to the upper dashed black curve) is smaller than the value of $\kappa = 1.133$, such that the EMCF brought by the transducer is larger than the optimal required one. This one can be estimated by $\tilde{\kappa}_{\text{opt0}} = 0.7678$, corresponding to the value of $\kappa$ leading to the best performance, and associated to the red curve in Fig. 20(a).

In order to experimentally test this case, it is possible to degrade the EMCF by adding an inductance $L_s$ in the shunt, *i.e.* in series with $R$. This stems from Eq. (5) in which $L_t$ at the denominator is replaced by $L_t + L_s$. To degrade the EMCF to $\kappa = \tilde{\kappa}_{\text{opt0}} = 0.7678$, one needs a total inductance of $L_t + L_s = 1431.34$ µH in the shunt. This is obtained thanks to the real-time controller that is programmed to simulate an inductance $L_s = 774.3$ µH using the amplifier in voltage mode, as illustrated in Fig. 24. It involves measuring the electric current $\dot{Q}(t)$ in the transducer thanks to the monitor of the amplifier and computing in real time the voltage $V(t) = R_s\dot{Q} + L_s\ddot{Q}$ that is applied to the terminals of the transducer to emulate the behaviour of an inductance $L_s$ in series with a resistance $R_s$. It should be noted that inductances are usually simulated using current-mode amplifiers, where a voltage signal is integrated over time to avoid derivation which induces noise in the signal. However, in this case, the transducer behaves as a current source due to its inductive nature. Therefore, it is not feasible to connect a current-mode amplifier (which also acts as a current source) in series with the transducer. This constraint necessitates the use of a voltage-mode amplifier for inductance simulation. The amplifier includes a built-in low-pass filter with a cutoff frequency set to 1 kHz, which attenuates the high-frequency noise amplified by the derivative action.

With the optimal $\tilde{\kappa}_{\text{opt}}$ parameter, one has to obtain the associated parameters $\tilde{\omega}_2^{\text{opt}}$ and $\tilde{\tau}_e^{\text{opt}}$, thanks to Eq. (36) and Fig. 20(a), giving $\tilde{\omega}_2^{\text{opt}} = 0.8864\omega_1$ and $\tilde{\tau}_e^{\text{opt}} = 0.6298/\omega_1$, leading to $\tilde{\omega}_2^{\text{opt}}/(2\pi) = 23.66$ Hz and the resistance of the circuit $R_{\text{opt}} = R_t + R_s = 0.3811\ \Omega$. The natural frequency of the DVA is adjusted by changing the length of the cantilever beam. Moreover, since $R_{\text{opt}} < R_t$, and a negative resistance $R_s$ is simulated by the real time controller.

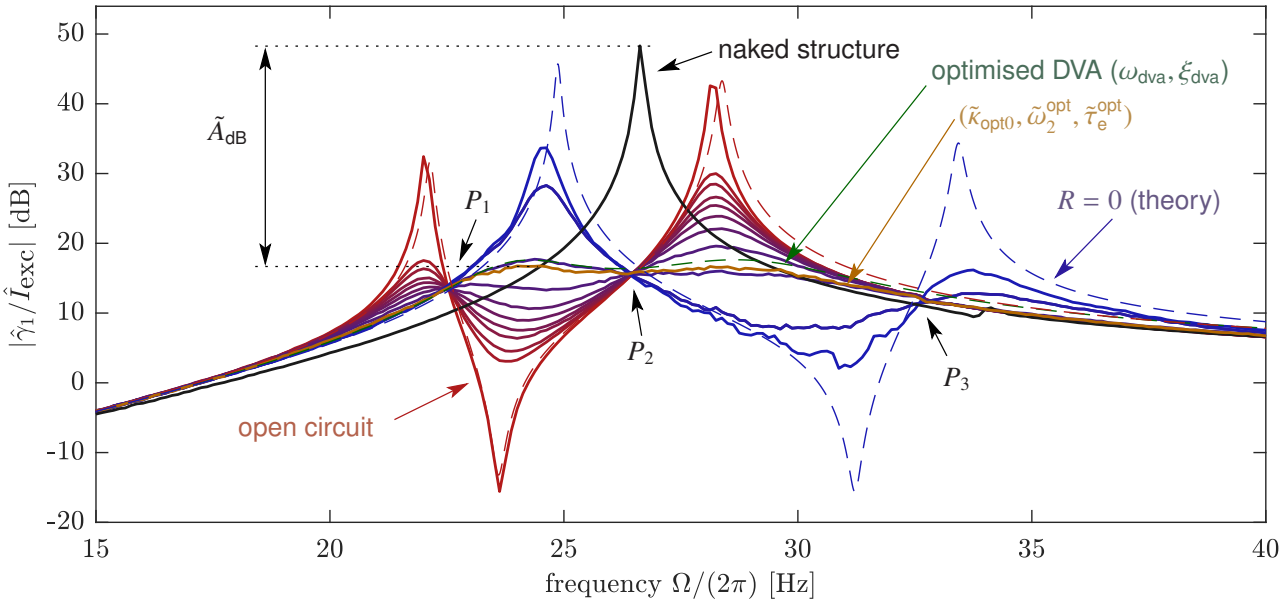



**Fig. 25:** Experimental modulus of FRF $\hat{\gamma}_1/\hat{I}_{\text{exc}}$ of the mechanical structure under several conditions, with the natural frequency of the DVA and the electromechanical coupling optimised ($\omega_2 = \tilde{\omega}_2^{\text{opt}}$, $\kappa = \tilde{\kappa}_{\text{opt}}$). (black line): uncoupled primary structure (without DVA and EM-shunt) and (black dashed line) associated theoretical curve; (red line): transducer in open circuit; (gradient curve from red to blue): different values of $R_s$; (red dashed line): theoretical open circuit case; (blue dashed line): theoretical $R = 0$ case; (gold curve) optimal electrical time constant ($\tau_e = \tilde{\tau}_e^{\text{opt}}$); (green dashed line) theoretical optimised mechanical DVA case (its parameters follows Eqs. (37) and (38)).

Figure 25 compares the modulus of the structure's frequency response for different configurations, like in the previous section. The black curve still shows the FRF of the structure without absorber. The gradient curves from red to blue shows the different functions for different $R_s$ values, from the open circuit case in red to the short circuit case ($\tau_e \to +\infty$) in blue. All curves is obtained with the simulated inductance $L_s$. One can observe the presence of the three fixed points, with the external fixed point $P_1$ and $P_3$ approximately at the same amplitude.

The gold curve shows the FRF with the optimised DVA+R-shunt. Contrary to the previous case (see Fig. 23), the present optimal parameters ($\tilde{\kappa}_{\text{opt}}, \tilde{\omega}_2^{\text{opt}}$, and $\tilde{\tau}_e^{\text{opt}}$) give a FRF with 3 extrema. One observes that it is very close (and slightly below) the one of an optimised mechanical DVA, shown in dashed green. As predicted by the theory, the

DVA+R-shunt, with its three parameters $(\omega_2, \kappa, \tau_e)$ optimised, shows slightly better performances than a mechanical DVA. It can be read that $\tilde{A}_{\text{dB}} = 31.6\ \text{dB}$, in full agreement with Fig. 17(b).

# 6 Conclusion

This study introduces a new method to replace the damping element of a mechanical DVA by a resistive shunt (R-shunt). It is shown that the R-shunt is not exactly equivalent to a simple viscous damper (dashpot) since it adds a new pole in the mechanical frequency response function (FRF). In analogy to a standard primary structure whose a mechanical DVA, which FRF shows two fixed points, in the case of the present DVA+R-shunt absorber, the FRF shows three fixed point. However, an $H_\infty$-optimisation is still possible and thoroughly conducted in the present study. As in a standard mechanical DVA, for which the two independent parameters (its natural frequency and damping ratio) are optimally known as a function of the mass ratio $\mu$, it is shown that the three parameters of the DVA+R-shunt absorber (the DVA's natural frequency, the electromechanical (EM) coupling factor of the EM transducer and the electrical tome constant, related to the shunt resistance) can be optimally chosen, also as a sole function of $\mu$. Interestingly, it is shown that an optimally tuned DVA+R-shunt absorber performs equivalently (or even slightly better) than an optimally tuned mechanical DVA, such that the proposed solution is perfectly successful in this case. It is still the case for a lightly damped DVA. However, if the DVA has naturally a large damping ratio, an other optimisation of the R-shunt must be performed, a question left for future investigations. It should also be noted that the internal resistance of the electromagnetic transducer is typically large compared to the optimal shunt resistance, which represents a technological limitation for a fully passive implementation. The study was conducted for both displacement and acceleration FRF amplitude reduction, yielding comparable performance in each case, though with different optimal electromechanical parameters. Finally, experimental successful validations focused on the reduction of the acceleration of a given resonance of a laboratory structure.

# Authors' Contributions

G. Hay carried out the conceptualisation, data curation, formal analysis, experimental work and the writing and revision of the original draft. C. Giraud-Audine contributed to the conceptualisation and set up the real-time controller. O. Thomas originated the main idea for the study, and contributed to the conceptualization, formal analysis, and the revision of the original draft. All authors reviewed and approved the final manuscript.

# Acknowledgements

The authors warmly thank the reviewers for their constructive comments and especially one of them for her/his ideas which lead to substantial contributions in the final version of the article, for providing the closed-form expressions of Appendix A and stimulating the discussions of Sections 2.2 and 3.2.4.

# Appendix

# A Analytical resolution of $\omega_2^{\text{opt}}$ for the displacement case

In the Section 3.1, the optimisation of the DVA natural frequency $\omega_2$ was first carried out numerically, before an analytical expression was derived from the analysis of the results, in particular the position of the fixed point $\Omega_{P_2}$. A subsequent analysis revealed an algebraic method for determining the value of $\omega_2$ that enforces equal amplitudes at the two outer fixed points $P_1$ and $P_3$.

This method relies on the *resultant*, an algebraic elimination tool that removes a variable between two polynomials while preserving their common roots. Specifically, the resultant of two polynomials $P$ and $Q$ with respect to a variable $x$, denoted $\text{Res}_x(P, Q)$, is defined as the determinant of the associated Sylvester matrix. It vanishes if and only if the two polynomials share a common root in $x$.

In the present problem, $\Omega_{P_1}$ and $\Omega_{P_3}$ are considered as roots of the polynomial appearing on the left-hand side of Eq. (16), denoted $P(X, \omega_2)$. The objective is then to successively eliminate the variables $\Omega_{P_1}$ and $\Omega_{P_3}$ so as to obtain a condition expressed solely in terms of $\omega_2$.

To this end, the following auxiliary function is introduced:

$$h(\Omega_{P_1}, \Omega_{P_3}, \omega_2) = \frac{A(\Omega_{P_3}, \omega_2)\, C(\Omega_{P_1}, \omega_2) - A(\Omega_{P_1}, \omega_2)\, C(\Omega_{P_3}, \omega_2)}{\Omega_{P_1}^2 - \Omega_{P_3}^2} \tag{A.1}$$

where the functions $A$ and $C$ are defined in Eq. (10a) and Eq. (10c), respectively. This symmetrised construction serves as an elimination device: it cancels the trivial contributions associated with the case $\Omega_{P_1} = \pm\,\Omega_{P_3}$ and retains only the configurations in which the two frequencies correspond to distinct solutions of the system.

The resultant procedure is then applied successively to eliminate the variables $\Omega_{P_1}$ and $\Omega_{P_3}$:

$$\mathrm{Res}_{\Omega_{P_3}}\Big(P(\Omega_{P_3}, \omega_2),\ \mathrm{Res}_{\Omega_{P_1}}\big(P(\Omega_{P_1}, \omega_2),\ h(\Omega_{P_1}, \Omega_{P_3}, \omega_2)\big)\Big). \tag{A.2}$$

This operation amounts to projecting the original system onto an equation depending solely on $\omega_2$, by eliminating all intermediate variables while preserving the compatibility conditions of the system. The optimal value is then obtained directly:

$$\omega_2^{\mathrm{opt}} = \omega_1 \sqrt{\frac{1}{1+\mu} - \frac{\kappa^2}{2}} \tag{A.3}$$

This expression then allows the frequencies associated with the three fixed points to be determined:

$$\Omega_{P_1,P_3} = \omega_1 \sqrt{1 \pm \frac{\sqrt{(\mu+1)\,(\kappa^4(\mu+1)^2 + 4\mu)}}{2(1+\mu)}}, \tag{A.4}$$

and

$$\Omega_{P_2} = \omega_1 \sqrt{\frac{1}{1+\mu}}. \tag{A.5}$$

This recovers the frequency of the central fixed point $P_2$, as defined in Eq. (22) from the analysis of the numerical simulations. From these expressions, the critical value of the parameter $\kappa$ for which the amplitude at $P_2$ exceeds those at $P_1$ and $P_3$ can be determined:

$$\kappa = \sqrt[4]{\frac{4\mu}{(\mu+1)^3}}. \tag{A.6}$$

The dashed green curve associated with Eq. (A.6) (Fig. A.1) coincides with the numerical solution (dashed white curve) presented in Fig. 3.

# B Analytical resolution of $\tilde{\omega}_2^{\mathrm{opt}}$ for the acceleration case

Following the same approach as for the displacement case (see Appendix A), it is possible to determine the value of the DVA natural frequency such that the fixed points $P_1$ and $P_3$ reach the same amplitude. Applying the same method as for the displacement case yields:

$$\tilde{\omega}_2^{\mathrm{opt}} = \omega_1 \sqrt{\frac{1-\kappa^2}{2} + \frac{\sqrt{\kappa^4+1}}{2}}. \tag{B.1}$$

The frequencies of the fixed points satisfy the following relations:

$$\tilde{\Omega}_{P_1,P_3} = \frac{\omega_1}{2} \sqrt{(\mu+2)\Big(\sqrt{\kappa^4+1}+1\Big) \pm \sqrt{\mu(\mu+4)\Big(\sqrt{\kappa^4+1}+1\Big)^2 + 4\kappa^4}}, \tag{B.2}$$

and

$$\tilde{\Omega}_{P_2} = \omega_1, \tag{B.3}$$

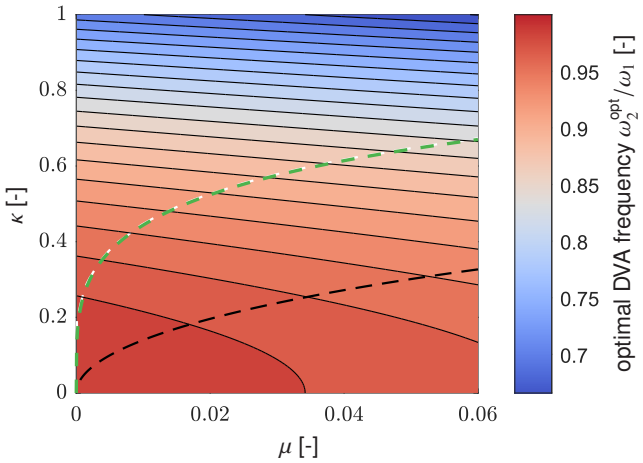



**Fig. A.1:** Evolution of the ratio $\omega_2^{\text{opt}}/\omega_1$ as a function of $\mu$ and $\kappa$, shown in Fig. 3. The dashed green curve corresponds to the function of $\kappa$ defined in Eq. (A.6), for which the value of the fixed point $P_2$ exceeds those of the corrected fixed points $P_1$ and $P_3$.

the latter being consistent with the value obtained from the numerical simulations (see Eq. (35)). From these expressions, the critical value of $\kappa$ for which the amplitude at the fixed point $P_2$ exceeds those at the fixed points $P_1$ and $P_3$ is determined as:

$$\kappa = \sqrt{\frac{2\mu}{1-\mu}}. \tag{B.4}$$

The dashed green curve associated with Eq. (B.4) (Fig. B.1) coincides with the numerical solution (dashed white curve) presented in Fig. 19.

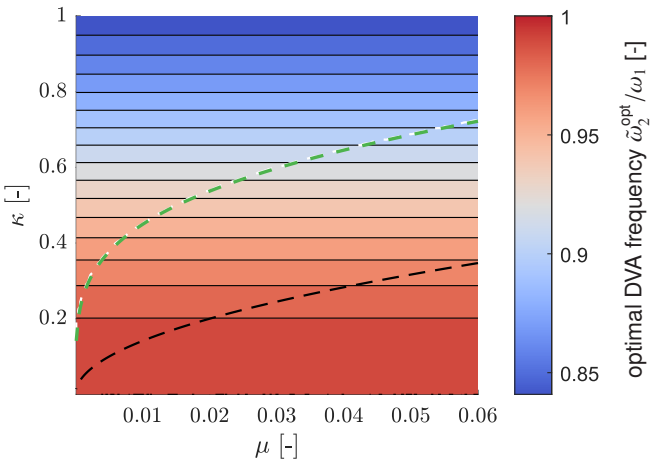



**Fig. B.1:** Evolution of the ratio $\tilde{\omega}_2^{\text{opt}}/\omega_1$ as a function of $\mu$ and $\kappa$, shown in Fig. 19. The dashed green curve corresponds to the function of $\kappa$ defined in Eq. (B.4), for which the value of the fixed point $P_2$ exceeds those of the corrected fixed points $P_1$ and $P_3$.

# References

[1] F. Lanchester. Damping torsional vibrations in crank-shafts, January 1914, URL https://www.google.com/patents/US1085443. US Patent 1,085,443.

[2] J. C. Snowdon. *Vibration and shock in damped mechanical systems*. John Wiley & Sons, 1968.

[3] M. Vakilinejad, A. Grolet, and O. Thomas. A comparison of robustness and performance of linear and nonlinear lanchester dampers. *Nonlinear Dynamics*, 100:269–287, 2020. doi:10.1007/s11071-020-05512-x.

[4] F. Frahm. Device for damping vibrations of bodies., October 1909, URL https://patents.google.com/patent/US989958A/en. US Patent 989,958.

[5] V. Mahé, A. Grolet, H. Mahé, and O. Thomas. Dynamic stability of centrifugal pendulum vibration absorbers allowing a rotational mobility. *Journal of Sound and Vibration*, 517:116525, 2022. doi:10.1016/j.jsv.2021.116525.

[6] M. Auleley, C. Giraud-Audine, H. Mahé, and O. Thomas. Tunable electromagnetic resonant shunt using pulse-width modulation. *Journal of Sound and Vibration*, 500:116018, 2021.

[7] G. Hay, C. Giraud-Audine, H. Mahé, and O. Thomas. Torsional vibrations reduction on an elastic rotating structure by an electromagnetic antiresonance shunt using a dc motor. *Journal of Sound and Vibration*, 2025. Submitted.

[8] J. P. Den Hartog. *Mechanical vibrations*. Courier Corporation, 1985.

[9] S. Krenk and J. Høgsberg. Tuned mass absorber on a flexible structure. *Journal of Sound and Vibration*, 333:1577–1595, 2014.

[10] J. Connor and S. Laflamme. *Structural Motion Engineering*. Springer, 2014.

[11] T. Konar and A. D. Ghosh. A review on various configurations of the passive tuned liquid damper. *Journal of Vibration and Control*, 29(9-10):1945–1980, 2023.

[12] F. Foti and L. Martinelli. Hysteretic behaviour of stockbridge dampers: Modelling and parameter identification. *Mathematical Problems in Engineering*, page ID 8925121, 2018.

[13] L. Y. W. Xu, Z. Hu, and L. Xiao. A novel dynamic vibration absorber for vibration control of piping systems under multi-frequency harmonic excitations. *Scientific reports*, 15:2086, 2025.

[14] K. Jaboviste, E. Sadoulet-Reboul, O. Sauvage, and G. Chevallier. A framework for the design of rotating multiple tuned mass damper. In *Topics in Modal Analysis & Testing, Volume 8: Proceedings of the 38th IMAC, A Conference and Exposition on Structural Dynamics*, pages 393–397, 2021.

[15] G. Huo, Z. Chen, Y. Jiao, and X. Zhu. Optimization of dynamic vibration absorbers for suppressing sound radiation of plate structures. *Journal of Vibration and Acoustics*, 143:021003, 2020.

[16] R. L. Forward. Electronic damping of vibrations in optical structures. *Appl. Opt.*, 18(5):690–697, 1979.

[17] N. Hagood and A. von Flotow. Damping of structural vibrations with piezoelectric materials and passive electrical networks. *Journal of Sound and Vibration*, 146(2):243–268, 1991.

[18] S. Behrens, A. J. Fleming, and S. Moheimani. Passive vibration control via electromagnetic shunt damping. *IEEE/ASME transactions on mechatronics*, 10(1):118–122, 2005.

[19] O. Thomas, J. Ducarne, and J.-F. Deü. Performance of piezoelectric shunts for vibration reduction. *Smart Materials and Structures*, 21(1):015008, 2011.

[20] M. Berardengo, S. Manzoni, O. Thomas, and M. Vanali. Guidelines for the layout and tuning of piezoelectric resonant shunt with negative capacitances in terms of dynamic compliance, mobility and accelerance. *Journal of Intelligent Material Systems and Structures*, 32:2092–2107, 2021.

[21] T. Inoue, Y. Ishida, and M. Sumi. Vibration suppression using electromagnetic resonant shunt damper. *Journal of Vibration and Acoustics*, 130(4):041003, 2008.

[22] X. Tang, Y. Liu, W. Cui, and L. Zuo. Analytical solutions to h 2 and $h_\infty$ optimizations of resonant shunted electromagnetic tuned mass damper and vibration energy harvester. *Journal of Vibration and Acoustics*, 138(1):011018, 2016.

[23] M. Auleley, O. Thomas, C. Giraud-Audine, and H. Mahé. Enhancement of a dynamic vibration absorber by means of an electromagnetic shunt. *Journal of Intelligent Material Systems and Structures*, 32(3):331–354, 2021.

[24] R. Sun, W. Wong, and L. Cheng. Optimal design of a tunable electromagnetic shunt damper for dynamic vibration absorber. *Mechatronics*, 83:102763, 2022.

[25] P. Bonello, S. Rafique, and R. Shuttleworth. A theoretical study of a smart electromechanical tuned mass damper beam device. *Smart Material and Structures*, 21(12):125004, 2012.

[26] J. Hogsberg. Vibration control by piezoelectric proof-mass absorber with resistive-inductive shunt. *Mechanics of Advanced Materials and Structures*, (2):141–153, 2021.

[27] W. Sheng and H. Xiang. A piezoelectric tuned mass damper for simultaneous vibration control and energy harvesting. *Smart Materials and Structures*, 33(1):015019, 2023.

[28] N. Anh, V. Tuan, P. Thang, and N. Linh. Extension of the fixed point theory to tuned mass dampers with piezoelectric stack energy harvester. *Journal of Sound and Vibration*, 581:118411, 2024.

[29] S. Zhu, W. Shen, and Y. Xu. Linear electromagnetic devices for vibration damping and energy harvesting: Modeling and testing. *Engineering Structures*, 34:198–212, 2012.

[30] L. Zuo and W. Cui. Dual-functional energy-harvesting and vibration control: electromagnetic resonant shunt series tuned mass dampers. *Journal of vibration and acoustics*, 135(5):051018, 2013.

[31] J.-S. Bae, J.-H. Hwang, J.-H. Roh, J.-H. Kim, M.-S. Yi, et al. Vibration suppression of a cantilever beam using magnetically tuned-mass-damper. *Journal of Sound and Vibration*, 331(26):5669–5684, 2012.

[32] F. Bourquin, G. Caruso, M. Peigney, and D. Siegert. Magnetically tuned mass dampers for optimal vibration damping of large structures. *Smart Materials and Structures*, 23(8):085009, 2014.

[33] A. F. Vakakis and O. Gendelman. Energy pumping in nonlinear mechanical oscillators: Part ii - resonance capture. *Journal of Applied Mechanics*, 68:42–48, 2001.

[34] Z. Lu, Z. Wang, Y. Zhou, and X. Lu. Nonlinear dissipative devices in structural vibration control: A review. *Journal of Sound and Vibration*, 423:18–49, 2018.

[35] A. S. Saeed, R. A. Nasar, and M. A. Al-Shudeifat. A review on nonlinear energy sinks: designs, analysis and applications of impact and rotary types. *Nonlinear Dynamics*, 111:1–37, 2023.

[36] X.-F. G. anf H. Ding, J.-C. Ji, K.-X. Wei, X.-J. Jing, and L.-Q. Chen. A state-of-the-art review on the dynamic design of nonlinear energy sinks. *Engineering Structures*, 313:118228, 2024.

[37] P.-O. Mattei and R. Côte. Optimization of a dynamic absorber with nonlinear stiffness and damping for the vibration control of a floating offshore wind turbine toy model. *Journal of Theoretical, Computational and Applied Mechanics*, may 2023. doi:10.46298/jtcam.10123.

[38] K. Dekemele, C. Giraud-Audine, and O. Thomas. A piezoelectric nonlinear energy sink shunt for vibration damping. *Mechanical Systems and Signal Processing*, 220:111615, 2024. doi:10.1016/j.ymssp.2024.111615.

[39] J. A. Ignacio da Silva, L. Sanches, G. Michon, and F. D. Marques. An enhanced nonlinear energy sink for hybrid bifurcation passive mitigation and energy harvesting from aeroelastic galloping phenomena. *Journal of Computational and Nonlinear Dynamics*, 19(4):041004, 2024.

[40] A. Batou and S. Adhikari. Optimal parameters of viscoelastic tuned-mass dampers. *Journal of Sound and Vibration*, 445: 17–28, 2019.

[41] ANSI/IEEE Std 176-1987. *IEEE Standard on Piezoelectricity*. The Institute of Electrical and Electronics Engineers, Inc., 1988.

[42] S. Krenk. Frequency analysis of the tuned mass damper. *Journal of Applied Mechanics*, 72(6):936–942, 2005.

[43] J. Ducarne, O. Thomas, and J.-F. Deü. Structural vibration reduction by switch shunting of piezoelectric elements: modelling and optimization. *Journal of Intelligent Materials Systems and Structures*, 21(8):797–816, 2010. doi:10.1177/1045389X10367835.

[44] M. Berardengo, O. Thomas, C. Giraud-Audine, and S. Manzoni. Improved resistive shunt by means of negative capacitance: new circuit, performances and multi-mode control. *Smart Materials and Structures*, 25(7):075033, 2016. doi:10.1088/0964-1726/25/7/075033.

[45] D. J. Inman. *Engineering Vibration*. Pearson, 4th edition, 2014.

[46] K. C. S. Kwok, P. A. Hitchcock, and M. D. Burton. Perception of vibration and occupant comfort in wind-excited tall buildings. *Journal of Wind Engineering and Industrial Aerodynamics*, 97:368–380, 2009.

[47] J. Štěpánek and J. Máca. Optimization of tuned mass dampers attached to damped structures-minimization of maximum displacement and acceleration. *Acta Polytechnica CTU Proceedings*, 30:98–103, 2021.

[48] K. McConnell. *Vibration Testing: Theory and Practice*. Wiley, 1995.